EMBRY-RIDDLE
Aeronautical University™
SCHOLARLY COMMONS

Spring 5-2016

An Experimental Study of Momentum-Driven Unsteady Jets

Sravan Kumar Artham
Embry-Riddle Aeronautical University

An Experimental Study of Momentum-Driven

Unsteady Jets

A Thesis

Submitted to the Faculty

of

Embry-Riddle Aeronautical University

by

Sravan Kumar Artham

In Partial Fulfillment of the

Requirements for the Degree

of

Master of Science in Aerospace Engineering

May 2016

Embry-Riddle Aeronautical University
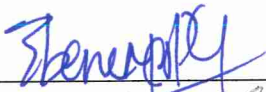
Daytona Beach, Florida

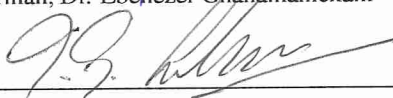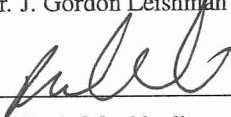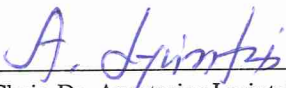An Experimental Study of Momentum-Driven Unsteady Jets

by

Sravan Kumar Artham

A Thesis prepared under the direction of the candidate's committee chairman, Dr. Ebenezer Gnanamanickam, Department of Aerospace Engineering, and has been approved by the members of the thesis committee. It was submitted to the School of Graduate Studies and Research and was accepted in partial fulfillment of the requirements for the degree of Master of Science in Aerospace Engineering

THESIS COMMITTEE

_____
Chairman, Dr. Ebenezer Gnanamanickam

_____
Member, Dr. J. Gordon Leishman

_____
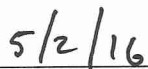Member, Dr. Reda Mankbadi

_____
Department Chair, Dr. Anastasios Lyrintzis
or Graduate Program Coordinator, Dr. Eric Perrell

4/29/16
_____
Date

_____
Dean of College of Engineering, Dr. Maj Mirmirani

4/29/2016
_____
Date

_____
Associate VP for Academics, Dr. Christopher Grant

5/2/16
_____
Date

ACKNOWLEDGMENTS

This thesis is an opportunity given to me by Embry-Riddle Aeronautical University. It was an unique experience to me which taught me many lessons. I'm greatly indebted to my parents, Venkat Sai Prasad Artham and Malleshwari Artham, for their love and continuous support to pursue my interests in life. This thesis could not have been successfully completed without a great deal of guidance. Last few months have proven to be challenging period in my life.

Special acknowledgement is due to many people who have supported me in completion of this thesis. I'm grateful to my advisor Dr. Gnanamanickam at Embry Riddle Aeronautical University who taught me many significant lessons for improvement.

I would like to thank my co-advisor and thesis committee member, Dr. J. Gordon Leishman for his valuable suggestions and for allowing me to use his test facility to conduct my experiment. I would like to thank Bill Russo and Mike Potash for helping me set-up the experiment.

A very special thanks to Dr. Zheng Zhang for his support and suggestions. I would also like to thank my friends: Bhushan, Rama Krishna, Harsha, Vikas, Niranjan, Sanjay. I couldn't have completed this thesis without your support.

Finally I wish to thank the Aerospace department at Embry-Riddle Aeronautical University for giving me this opportunity and funding for the project.

TABLE OF CONTENTS

LIST OF FIGURES

SYMBOLS

d	Hydraulic diameter of nozzle, m
m	Mass, kg
P	Dimensionless parameter based on cube root of puff volume
Re	Reynolds number, $V_j d/v$
r	Radial position, m
r_o	Center of the puff, m
$r_{1/2}$	Jet half radius, m
U	Mean axial velocity, ms^{-1}
U	Axial velocity, ms^{-1}
$U_{r_{1/2}}$	Velocity at jet half radius, ms^{-1}
U_c	Time averaged center-line velocity, ms^{-1}
u'	Fluctuations in axial direction, ms^{-1}
u_{rms}	Root mean square value of axial velocity, ms^{-1}
V	Radial velocity, ms^{-1}
V_j	Maximum velocity, ms^{-1}
V_{avg}	Mean of maximum velocities, ms^{-1}
v_{rms}	Root mean square value of radial velocity, ms^{-1}
v'	Fluctuations in axial direction, ms^{-1}

w' Fluctuations in azimuthal direction, ms^{-1}

x Axial direction, m

α Entrainment coefficient

θ Azimuthal direction

Δ_p Time between two puffs, s

δ Width of the jet, m

$\delta_{r_{V1}}$ Radial extent of the of the starting vortex corresponding to first puff

$\delta_{r_{V2}}$ Radial extent of the of the starting vortex corresponding to second

μ Dynamic viscosity, m^2s^{-1}

ρ Density kgm^{-3}

ABBREVIATIONS

DAQ   Data Acquistion

DP   Double puff

HWA   Hot Wire Anemometry

KHI   Kelvin Helmholtz Instability

PIV   Particle image velocimetry

SJ   Steady jet

SP   Single puff

ABSTRACT

Artham, Sravan Kumar MSAE, Embry-Riddle Aeronautical University, May 2016. An
Experimental Study of Momentum-Driven Unsteady Jets .

Jets are seen commonly in nature and engineering and can be broadly classified into
steady and unsteady jets. The study of unsteady jets has recieved little attention when
compared to its steady counterpart. A type of unsteady jet is the turbulent puff which is a
momentum driven jet in which fluid is ejected from a jet orifice intermittently. Common
examples of turbulent puff like jets are coughs and volcanoes. The studies on momentum
driven unsteady jets have primarily focused on single ejection events (single puffs) where
an instantaneous supply of momentum drives the source fluid downstream of a nozzle.
This work focuses on dual puffs in which two volumes of fluid (dual puffs), separated
by a time Δ_p are ejected from a jet orifice into ambient. An experimental framework to
study such dual puffs with varying separation and ejected volume was built. The dual puffs
studied were compared with both steady jets and single puffs. The mean velocity of these
flow fields were measured using hot-wire anemometry. Complementary flow visualizations
were also carried out. Dual puffs with Δ_p = 0.3 s, 0.5 s, 0.7 s ans 1.79 s were considered.
It was determined that for short time separations $\Delta_p V_j/d$ = 430, the dual puffs persisted for
longer distances when compared to a single puff or dual puffs with larger time separation
($\Delta_p V_j/d$ = 1540). Here V_j is the maximum jet exit velocity and the d the diameter of the
jet orifice. However, at large time separation ($\Delta_p V_j/d$ = 1540) the dual puffs expanded
considerably more rapidly than dual puffs with smaller separation or single puffs. This

indicates that the dual puff studied can be classified into two categories based on the time separation between the puffs. These observations are of an integral nature and a more detailed analysis of the flow field using advanced techniques as particle image velocimetry (PIV) are recommended to establish the precise flow physics leading to this behavior.

1. Introduction

A jet is a stream of fluid (liquid or gas) discharged from a narrow opening or a nozzle which expands over a distance usually much greater than the hydraulic diameter of the opening or nozzle (Bajpai, n.d.). Jets are classified into two types: 1) Steady jets (SJ) 2) Unsteady jets (UJ). Steady jets have continuous supply of momentum as it translates downstream whereas unsteady jets are formed when fluid exits an orifice such as a jet nozzle intermittently or with varying mass flow rate. Common example of a unsteady jet is the flow field caused by a human cough. The Reynolds number of this flow ranges from Re = 1,500 to 2,500 (Nishi et al., 2008). Here Reynolds number Re is defined as

$$Re = \frac{\rho V_j d}{\mu} \tag{1.1}$$

where, ρ is the density of the fluid, μ is the dynamic viscosity of the fluid, d is the diameter of the nozzle and V_j is the jet exit velocity. An example of a high Reynolds number turbulent puff is a volcano, which encapsulates fast moving hot gases mixed with rock. Volcanic gas clouds contain a mixture of solid particles of size approximately 10^{-3} mm which are toxic in nature and dangerous if inhaled directly (Parshley et al., 1982). This flow from a volcano is called pyroclastic flow (Parshley et al., 1982). The plumes are driven by buoyancy whereas the puffs are momentum-driven (Stewart & Turner, 1979). Volcanoes have

both momentum-driven and buoyancy-driven components (Fagents et al., 2013) and hence is a puff as well as a plume.

Puffs have clouds that can travel long distances, and in the case of coughs these act as agents for transmitting harmful pathogens (Bourouiba et al., 2014). A study on the transmission of cough clouds was carried out by Bourouiba et al. (2014), and it was determined that in the case of human coughs small droplets within the gas cloud travel much further away than expected. Another example of turbulent puffs are the flow field encountered in fuel injectors of a combustion chamber. Although the steady jet and its excited variant has been studied extensively, very little work has been carried out on the detailed flow physics of unsteady jets.
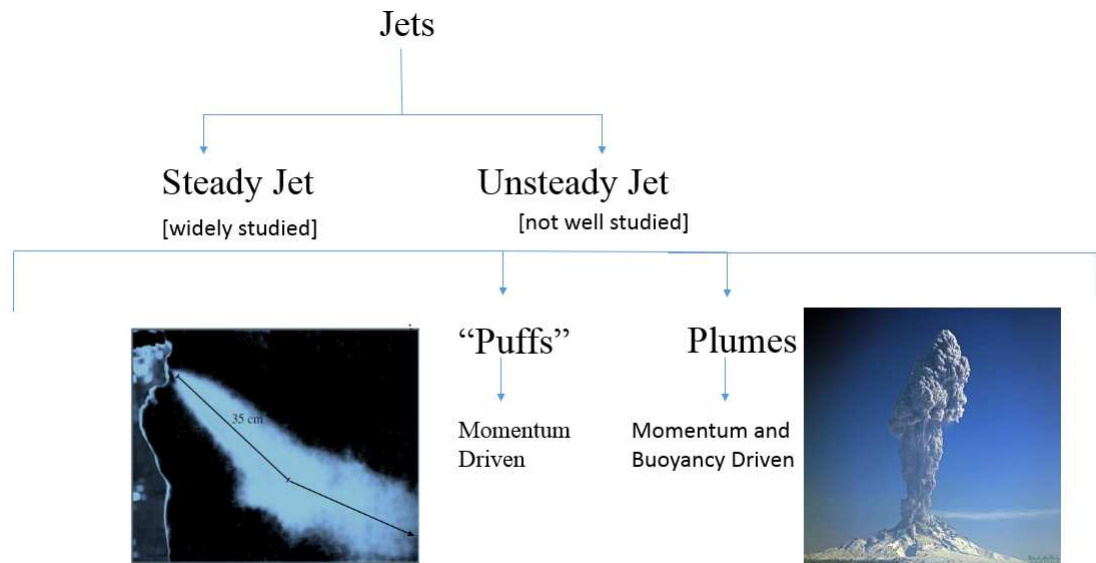
Figure 1.1. Classification of jets.

The obvious difference between a steady jet and an unsteady jet is clearly the continuous injection of air into the flow field in the case of a steady jet (Chojnicki et al., 2014).

This difference, however, results in the more rapid decay of the center line velocities with respect to downstream distance in unsteady jets than in steady jets. The entrainment of ambient air into the puffs happens further upstream than in a steady jet. Examining the flow field of a puff reveals two regions, namely laminar flow (outside the puff) and turbulent flow (within the puff) at the two edges of the puff, also called "front edge" and "back edge" as shown in Figs. 1.2 and 1.3. The x-axis shows the time and the y-ordinate shows the velocity variation. It is likely that the puff entrains fluid at the front and back edges along with its shear layer. The interaction between these two regions dictates the puff evolution. A clear understanding of turbulent puffs will help shed insight into its internal dynamics and thus its flow transport characteristics. However, if two puffs are ejected into ambient air with a short time interval, there is also an interaction between the two puffs. There has been very little work done to characterize these puffs. This work carries out some preliminary measurements to study the evolution of dual ejection events with varying time interval and compare them with single ejection events.
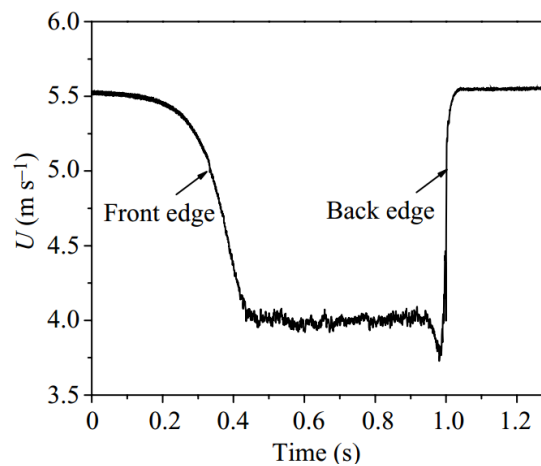
Figure 1.2. Front edge and back edge of the flow velocity of a puff (taken from Nishi et al. (2008)).
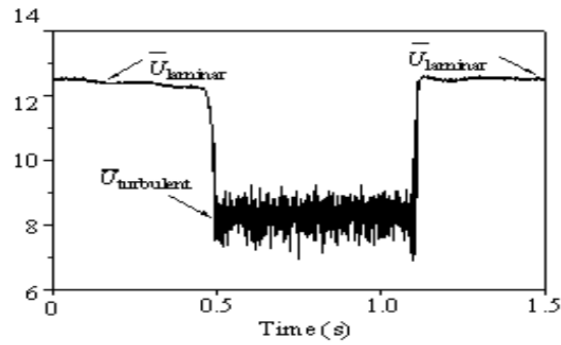
Figure 1.3. Laminar and turbulent regions of the puff (taken from Nishi et al. (2008)).

Figure 1.4. Flow visualization of a steady jet.

This thesis focuses on jets with a round nozzle (round jet) exits into still air. Polar coordinate system (x, r, θ) is used (see schematic of Fig. 1.5) where the mean velocity components are U, V and W in the streamwise, radial and azimuthal directions respectively. The corresponding fluctuations in the streamwise, radial and azimuthal directions are u', v', z' respectively.

1.1 Steady Axisymmetric Jets Exiting into still Air

Much of the literature on incompressible round jets is summarized in the review by Fellouah et al. (2009). Considering a circular jet with diameter d exiting the nozzle with some uniform velocity U, the width of the jet δ is observed to increase with downstream distance, as shown in Fig. 1.6. For a short distance downstream of the jet exit there is a region where the flow is potential, and this region is called the potential core as shown Fig. 1.6 (Fellouah et al., 2009). With increasing downstream distance, ambient fluid is entrained into the jet and the jet spreads out radially. This radial spreading continues with downstream distance resulting in reducing momentum within the jet, until the point where the viscous forces dissipate all the momentum leading to the destruction of the jet. With increasing downstream distance the entrained air also distorts the edge of the jet boundary, referred to as the shear layer (Fellouah et al., 2009). This distortion is because of the presence of vortical structures at the jet boundary, as shown in Fig. 1.6.

As the jet exits the nozzle, the high momentum fluid of the jet is sheared by the still ambient air resulting in the formation of vortical coherent structures. In Fig. 1.6, the distorted edge represents this shear layer between the higher momentum jet flow and the surrounding ambient fluid. These vortices roll up and pair up with increasing downstream distance, as shown in the Fig. 1.7. Two parameters namely the jet half radius $r_{1/2}$ and the time averaged diameter δ are used to characterize the edge and the spreading of the jet. The jet half radius $r_{1/2}$ is the radial distance where $U_{r_{1/2}} = U_c/2$ (Fellouah et al., 2009), where U_c is the centerline velocity (see Fig. 1.5).
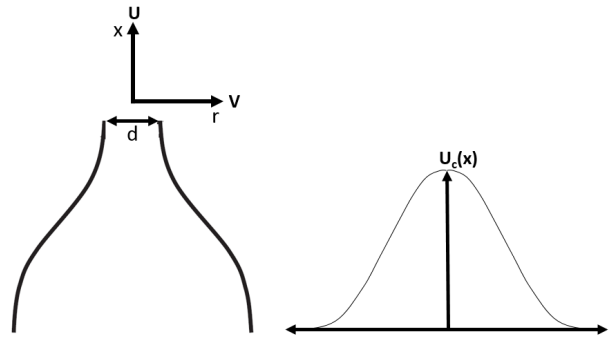
Figure 1.5. Coordinate system used in this thesis.
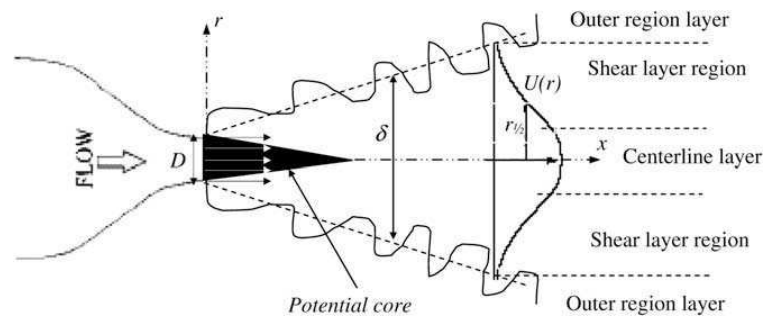
Figure 1.6. Schematic of an axisymmetric jet exiting from a nozzle (taken from Fellouah et al. (2009)).
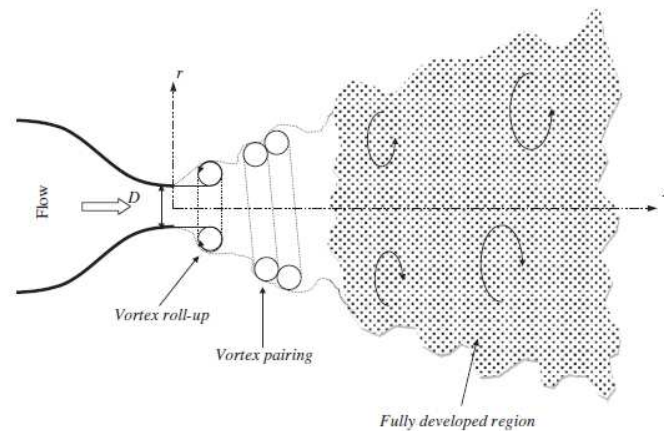
Figure 1.7. Vortex pairing observed in the flow field (taken from Fellouah et al. (2009)).

The jet can also be divided radially into three broad regions namely, 1. the centerline region, 2. the shear layer and 3. the outer layer (see Fig. 1.6). Maximum axial velocities at all downstream distances lie in the centreline region. The formation and pairing of the vortices are observed in the shear layer region. Throughout this process, there is energy transfer between turbulent structures of larger scales to smaller scales. Velocities in the outer layer, which are of order $U_c/10$, decrease to ambient values as $r \to \infty$. At $x/d \geqslant 70$ (far field) the flow is considered to be in equilibrium because the axial gradients are small compared to the radial gradients (thin shear layer approximation), and this region is called the fully developed region. The radial velocity distribution (see Fig. 1.8) of Wygnanski & Fiedler (1968) and Panchapakesan & Lumley (1993) have been recalculated by Fellouah et al. (2009) from the axial mean velocity profiles using the continuity equation:

$$\frac{1}{r}\frac{\partial}{\partial r}(r\rho V) + \frac{\partial}{\partial x}(\rho U) = 0 \tag{1.2}$$

In Eqn. 1.2 the second term corresponds to the axial component of velocity and the first term corresponds to the radial component. The assumption of no swirl of the mean velocity is used here which eliminates the θ component. The mean radial velocity is symmetric about the centerline because the flow expands laterally outward. Axial mean velocities normalized with respect to centerline velocities from various studies, as summarized by (Fellouah et al., 2009), are plotted in Fig. 1.9. Increase in width of the jet with respect to downstream distance is observed, corresponding to the decrease in initial jet momentum by entrainment of the ambient flow.
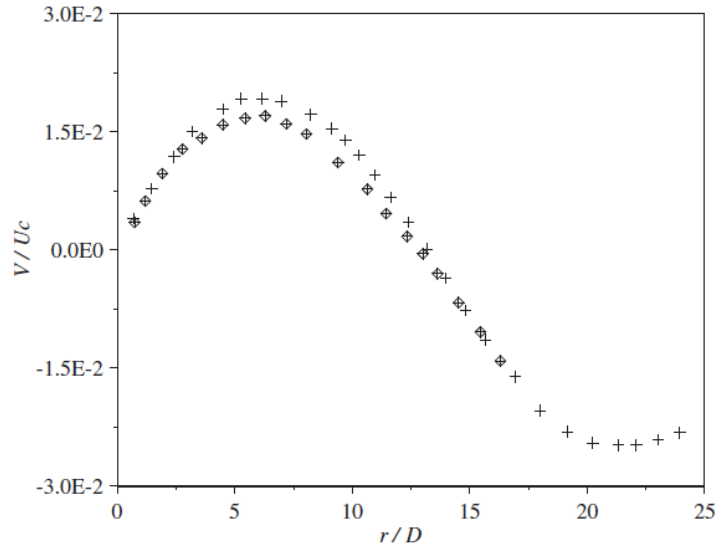
Figure 1.8. Normalised radial mean velocities. Both x-axis and y-axis (r/d and V/U_c respectively) are shown. Legend: ⊕ Wygnanski & Fiedler (1968); + Panchapakesan & Lumley (1993) as summarized by Fellouah et al. (2009) .

Considering the turbulent intensity, the flow field is divided into three regions, i.e., $x/d = 0 - 30$, $x/d = 30 - 60$ and $x/d = 60 - 100$. In the first region, from $x/d = 0 - 30$, there is an increase in turbulent intensity because of the coherent structures that are formed in the shear layer (Fellouah et al., 2009). This increment in intensity causes a decay in center line velocities. In the intermediate field from $x/d = 30 - 60$, the decay in the centerline velocities are more rapid than the self similar region because of the developing flow. Figure. 1.10 shows the downstream evolution of the axial and radial components of turbulent intensity as summarized by Fellouah et al. (2009). It can be seen that u'/U_c is greater than v'/U_c between $x/d = 0 - 20$. From $x/d = 60 - 100$ (far field), both the axial and radial turbulent intensity profiles tend to become constant along the streamwise direction (Fellouah et al., 2009). The jet is said to be in self-preserving state when all of it turbulent components are in equilibrium (Wygnanski & Fiedler, 1968).
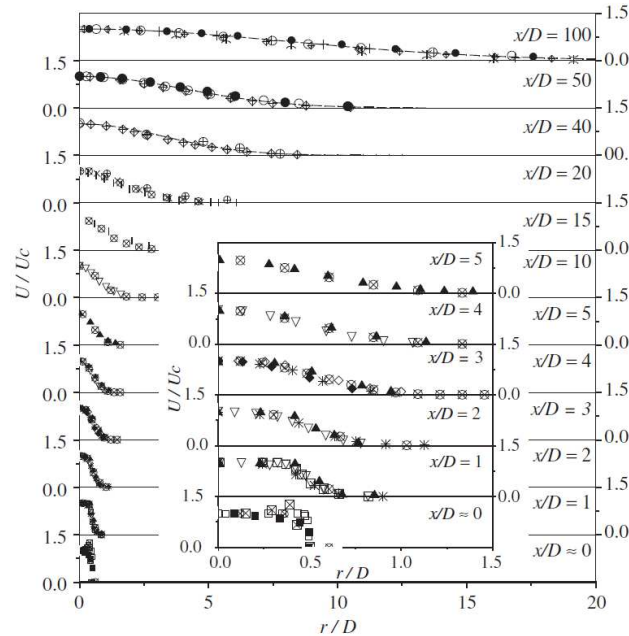
Figure 1.9. Normalized mean axial velocity profiles at different axial positions. Both x and y axis (r/D and U/U_c respectively) are shown. Legend: ⊕Wygnanski & Fiedler (1968); × Boguslawski & Popiel (1979); ⊠ Quinn & Militzer (1989); + Panchapakesan & Lumley (1993); ● Hussein et al. (1994); | Abdel-Rahman et al. (1997); ‡ Weisgraber & Liepmann (1998); □ Nobes et al. (2001); ■ Nobes et al. (2001); ⊠ Nobes et al. (2001); * Romano (2002); ◇ Xu & Antonia (2002); ▲ Iqbal & Thomas (2007); ⊗ Fellouah et al. (2009) as taken from Fellouah et al. (2009).

1.2   Turbulent Puffs

Consider now the case of a turbulent puff where a puff of fluid is ejected from a nozzle intermittently.

The velocity field of turbulent puffs was measured using Particle image velocimetry (PIV) by Ghaem-Maghami & Johari (2010). Puffs were generated by injecting air through a 5 mm diameter nozzle at Re = 5,000 (based on exit velocity) with the downstream measurement location being $40 - 75$ diameters (Ghaem-Maghami & Johari, 2010). The injected fluid was considered as cylinder with volume equal to volume of injected fluid. The base
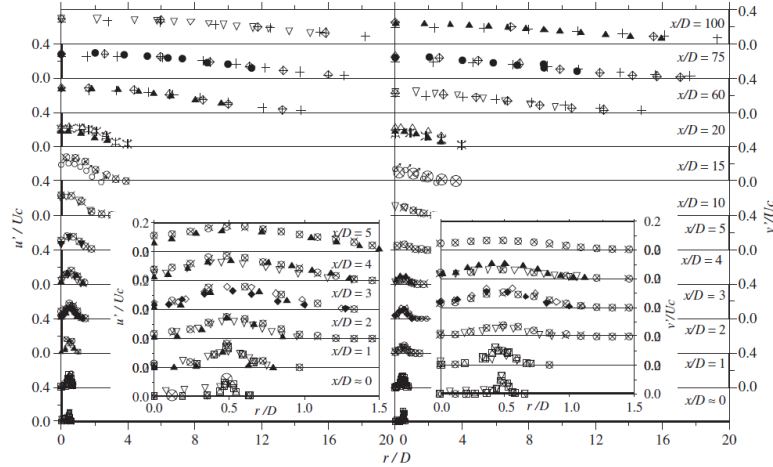
Figure 1.10. Axial and radial turbulent intensity profiles variation with downstream distance. Both x and y axis (r/D and u'/U_c, v'/U_c respectively) are shown. Legend: ⊕ Wygnanski & Fiedler (1968); ⊠ Chevray & Tutu (1978); × Boguslawski & Popiel (1979); ⬒ Quinn & Militzer (1989); + Panchapakesan & Lumley (1993);⊗ Fellouah et al. (2009); ⬓ Quinn & Militzer (1989); ◆ Xu & Antonia (2002); ▲ Iqbal & Thomas (2007); ● Hussein et al. (1994); ‡ Weisgraber & Liepmann (1998) as summarized by Fellouah et al. (2009).

diameter of the cylinder was considered to be the same as the hydraulic diameter of the nozzle. The length of the cylinder was calculated by the total volume injected Q over the nozzle area. P, a non-dimensional parameter is then defined as

$$P = (L/d)^{1/3} = (Q/Ad)^{1/3} \tag{1.3}$$

where L is the length of the cylinder and A is the area of the cylinder. For $P > 8$, flow behaves closer to a steady jet and for $P < 1.6$ the jet is essentially be flat cylinder or vortex rings. The mean velocity profiles for $P = 4, 5, 6, 8$ are shown in Fig. 1.11 where velocities are scaled with the center-line velocity U_c. Until the puff's half radius, the mean velocity profile matches that of the steady jet profile. These profiles were curve fitted by a Gaussian with k, r_o as fitting parameters using

$$U = U_c e^{(-k[(r-r_o)/r_{1/2}]^2)}. \tag{1.4}$$

Here, r_o is used to center the puff. The range of the fitting parameter k was found to be between 0.69 for $P = 4$ and 0.84 for $P = 8$ whereas the value of k for a steady jet was around 0.695.
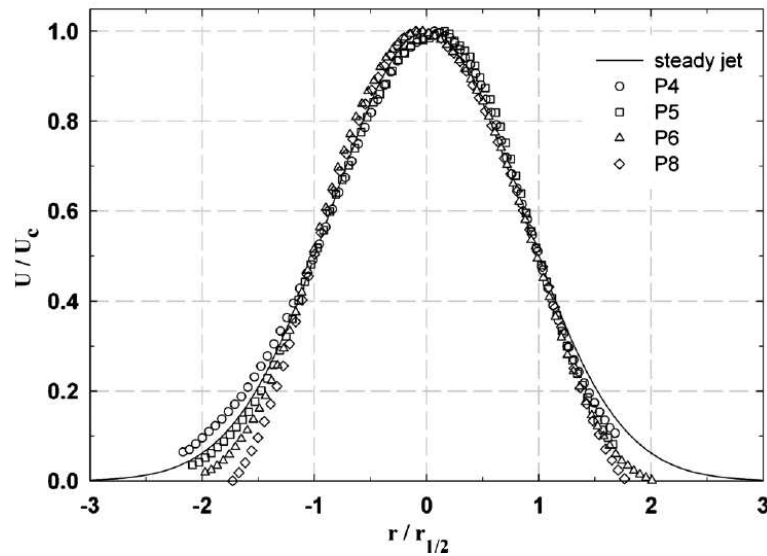
Figure 1.11. Axial velocity profile of steady jet and different number of puffs (taken from Ghaem-Maghami & Johari (2010)).

The radial profiles of axial velocity fluctuations u'_{rms} are scaled with the centerline velocity U_c and plotted against $r/r_{1/2}$ in Fig. 1.12. It is observed that they are symmetric about the centerline and $P = 4$ has the highest u'_{rms} with a peak value of $0.51 U_c$. Magnitude of u'_{rms}/U_c for $P = 4$ is is about twice the steady jet value. The profile for $P = 8$ puff approach the steady jet profile.
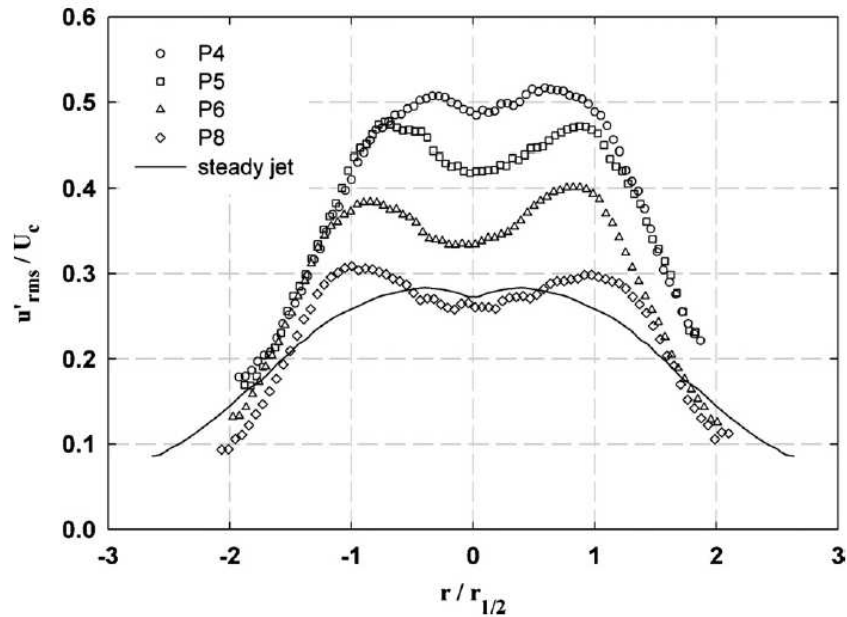
Figure 1.12. Axial fluctuation velocity profile of steady jet and puffs (taken from Ghaem-Maghami & Johari (2010)).

Radial velocity fluctuations are scaled in similarity coordinates and plotted against $r/r_{1/2}$, as shown in Fig. 1.13. Similar to that for the u'_{rms} profiles, the $P = 4$ puff has the highest v'_{rms} with a peak value of $0.43U_c$ among the four cases considered. The maximum magnitude of normalized radial fluctuation (v'_{rms}/U_c) for the $P = 4$ profile was found to be twice that of the steady case, and all the four profiles have higher values of v'_{rms}/U_c when compared to the steady jet case.

1.3   Coughs and Volcanoes

Work on puffs has also been carried by considering human coughs or volcanoes, these are two of the most commonly encountered turbulent puffs. A systematic study of these
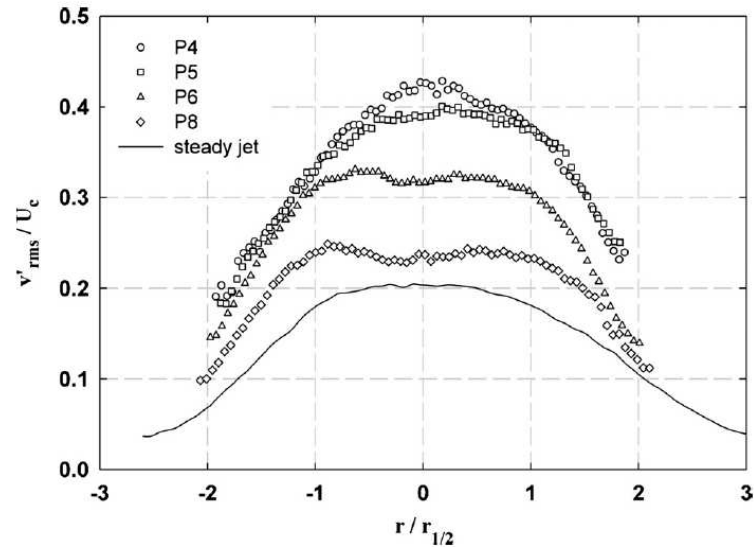
Figure 1.13. Radial fluctuation velocity profile of steady jet and puffs (taken from Ghaem-Maghami & Johari (2010)).

flows will help model these flows, where basic properties such as length and velocity scales, rate of spread, entrainment and effect of these parameters when subjected to external disturbances such as volumetric heating and body forces, can be better understood.

1.4   Studies on Cough and its Models

Kwon et al. (2012) characterized the exhalation velocity distribution while coughing and speaking. Measurements were carried out for 17 males and 9 females over a span of 210 and 420 ms. All the measurements were carried out using PIV. The male subjects coughed at an angle of around 38° and female subjects coughed at an angle of 32° . The mean velocities are decomposed as shown in Fig. 3.2. Here, the x-axis shows the mean velocity in the x-direction, i.e. u. The vertical velocities has been decomposed into two components v vertically up and down, as shown in Fig. 3.2. The averaged maximum u cough velocity

for males are 14.4 ms^{-1} while v is 5.2 ms^{-1} upward and -4.7 ms^{-1} downward. The resultant coughing velocity is 15.4 ms^{-1}. Averaged maximum u velocity for females is 10.1 ms^{-1} and v is 2.7 ms^{-1} upward, - 3.1 ms^{-1} downward and 10.78 ms^{-1} being the corresponding resultant velocity, which is 70% of resultant cough velocity found in males. The angle of upward and downward vectors with respect to the streamwise direction is shown in Fig. 3.2(a). These angles are 19.9° upward and 17.9° down for males and 15° upward and

(a) Cough Exhalation velocities.   (b) Speech Exhalation velocities
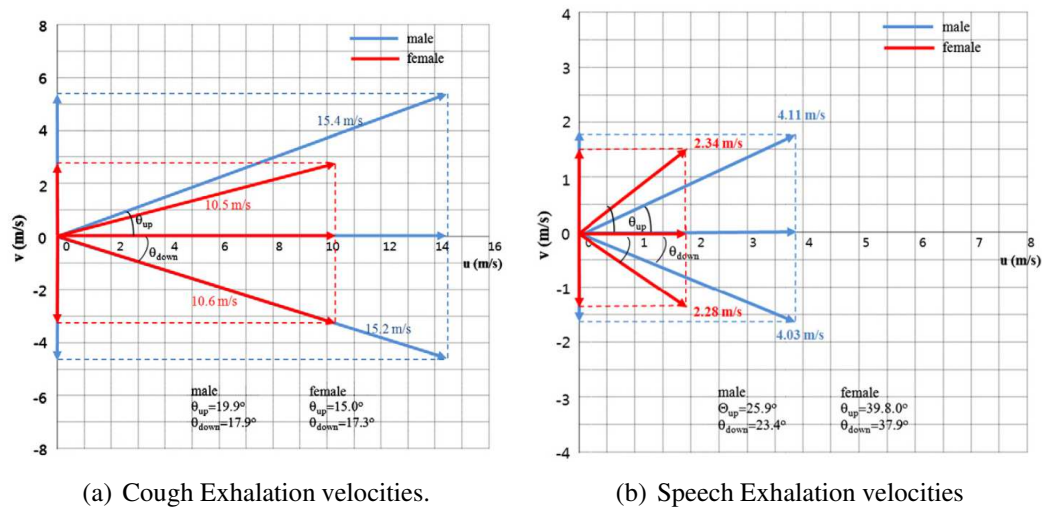
Figure 1.14. Resultant mean velocity distribution for males and females (Taken from Kwon et al. (2012)).

17.9° downward for females. A similar analysis of velocity distributions was conducted when words like *hana, dul*, etc., were pronounced by the test subject. The corresponding speaking velocity distribution is shown in Fig. 3.2.

Turbulent puffs pertaining to human coughs and human sneezes focusing on their multiphase nature was studied by Bourouiba et al. (2014). Visualization of human coughs and sneezes were conducted, and then used to develop a theoretical model to predict the trajectory of the coughs and sneezes. Interestingly, coughs and sneezes were found to have

a turbulent cloud of buoyant gas with suspended droplets, as shown in Fig. 1.15(a). The large droplets follow a ballistic trajectory and remain unaffected by the flow in gas phase, but smaller droplets (less than 50 μm) remain within the gas cloud. This outcome is shown in the streak image of Fig. 1.15(b). The period of a cough was around 200 – 500 ms (Gupta et al., 2009) with peak flows varying between 57 – 110 ms for female subjects and 57 – 96 ms for males.
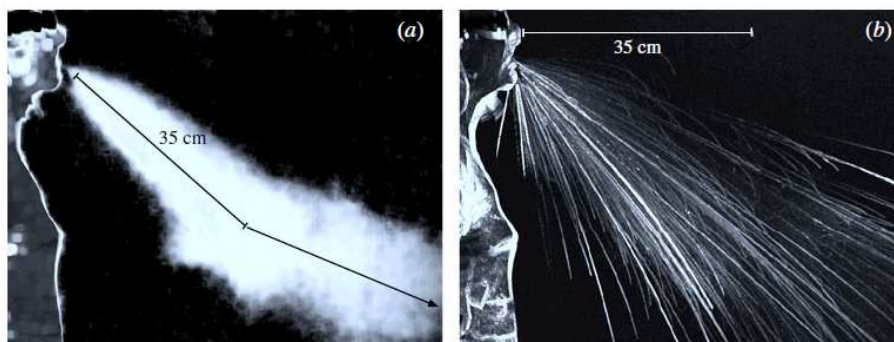
Figure 1.15. Buoyancy nature of sneeze cloud is observed figure-a. Trajectories of large droplets are shown in the streak image figure-b (As summarized from Bourouiba et al. (2014)).

High-speed image sequences of a sneeze recorded at 2000 fps is shown in Fig. 1.16. Total release time of the sneeze was 200 ms, and it can be seen that the smallest mist droplets remain suspended until the end of the image sequence. Circulation of the droplets in the cloud can be observed, and the direction of the pair of arrows indicated in Fig. 1.16 show that the cloud is moving upward (the effect of buoyancy).

The evolution of these violent, often involuntary respiratory events, i.e. a (cough or sneeze) is shown as a schematic in Fig. 1.17. As the droplet carrying buoyant momentum puff travels away from the source it entrains ambient air with increasing width and
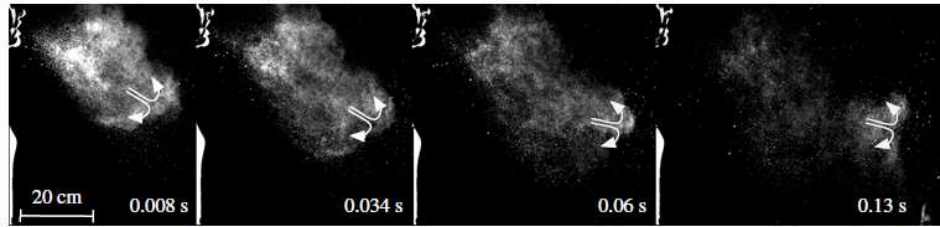
Figure 1.16. Effect of circulation being observed in the cough as summarized from Bourouiba et al. (2014).
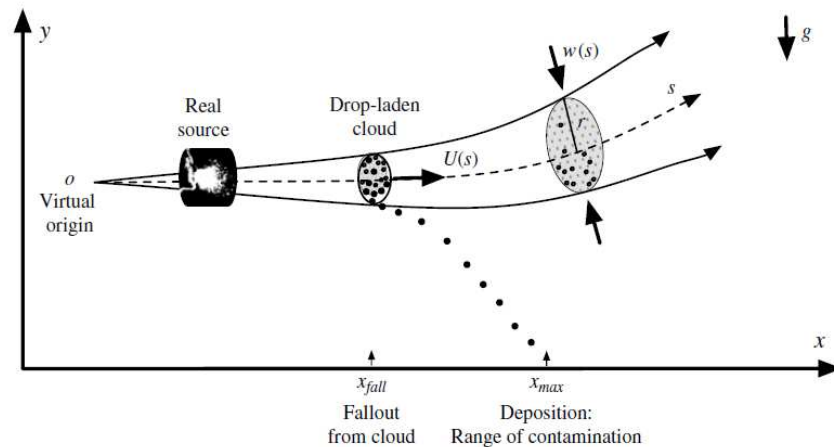
Figure 1.17. Evolution of a respiratory event moving horizontally from source. Droplets having negative buoyant force settle out at x_{fall} and reach final position x_{max} indicating the range of contamination, with $'o'$ being the virtual origin (as taken from Bourouiba et al. (2014)).

decreasing speed. As stated earlier, large droplets followed the trajectory of the cloud and smaller droplets remained recirculating until their speeds were in equilibrium within the surroundings. Analogous experiments were performed where the dynamics of turbulent, dyed, particle-laden fluid injected into a quiescent water tank was studied. A schematic of the experimental setup is shown in Fig. 1.18 (Bourouiba et al., 2014). The water tank was divided into two regions where the source piston was placed on one side and observation area where the flow was recorded on the other side. The Reynolds number of the puff was

around 5,000 with density between the two sections varying from 5.4 – 10 mg cm^{-3}. As the cloud progresses, entrainment is observed. which results in the increase in size and deceleration of the puff. The entrainment modifies the total mass and volume, but the shape is retained. The distance of the puff from the source, s, and jet half-width of the cloud, r, are related as shown in Fig. 1.19, where α is entrainment coefficient. Two phases of the puff were observed: The dynamics of first phase resembled that of a jet and the dynamics of the second phase was similar to that of a puff. In the first phase, until certain downstream axial location, the puff's momentum drives the puff forward, hence the jet like flow. With the dissipation of some momentum, buoyancy is the key factor enabling the puff to move forward (Bourouiba et al., 2014).
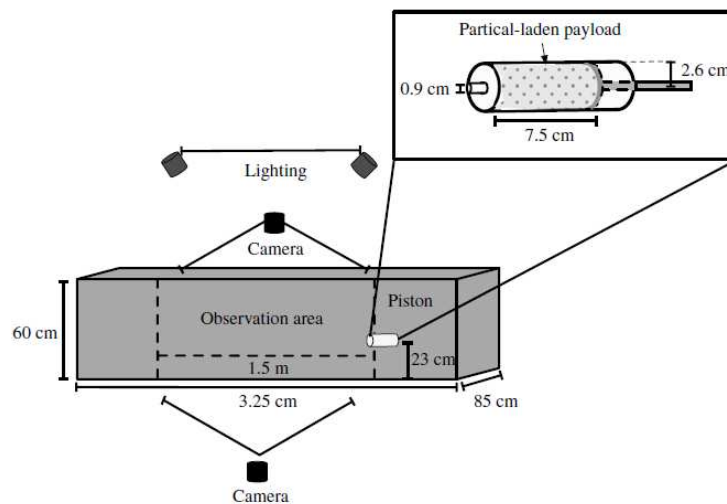
Figure 1.18. Experimental setup for dyed, particle-laden fluid injected into a water tank (taken from Bourouiba et al. (2014)).

$$r = \alpha s$$
$$V = \alpha U$$
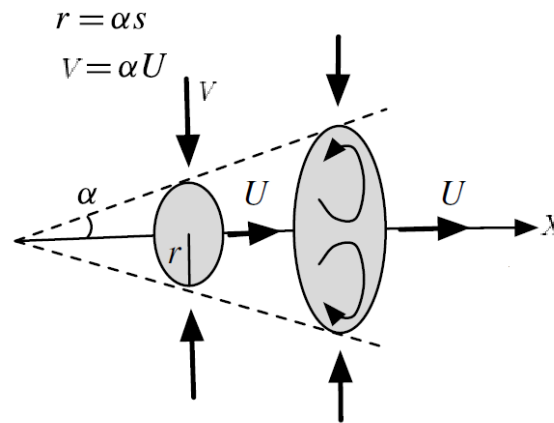
Figure 1.19. Illustration of the spreading of a puff with respect to axial location. V is the speed of ambient fluid being proportional to cloud speed U (taken from Bourouiba et al. (2014)).

1.5 Volcanic Model

During volcanic eruptions, a mixture of volcanic gas and pyroclasts exits from a vent with a net flow density being higher than the atmospheric density. As the eruption column mixes with the ambient air, the density of the eruption clouds reduces. The entrained air also expands by heating from the pyroclasts (Suzuki & Koyaguchi, 2010). If the amount of entrained air is sufficient, then the volcanic cloud convectively rises or else a heavy pyroclastic flow spreads on ground surface, as shown in Fig. 1.20. A three-dimensional, time dependent model that solves the conservation of mass, momentum, energy and thermodynamic state of pyroclasts exiting the vent was developed by Suzuki & Koyaguchi (2010) to calculate the properties of the eruption cloud. Simulations for explosive eruptions from a circular vent into ambient atmosphere were conducted, and time-averaged mean vertical velocity profiles were obtained (see Fig. 1.21).
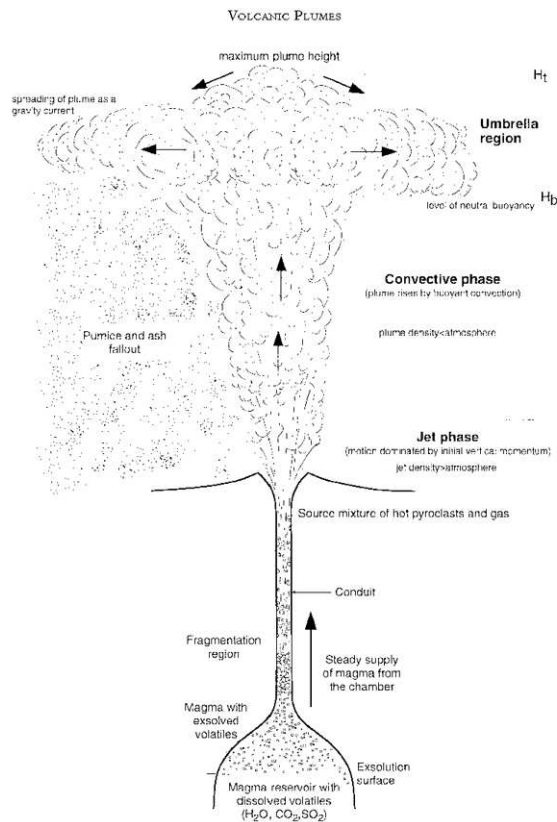
VOLCANIC PLUMES

Figure 1.20.Volcanic plume structure is shown. Effect of entrainment is observed with increasing height.

The eruption cloud from the vent exited with a density of 3.47 kgm^{-3}. The width of the eruption column was found to increase linearly with height, and after it reached a maximum height an umbrella cloud (see Fig. 1.20) spreads radially with the eruption column below being stable. The umbrella region has the entrained ambient air and toxic pyroclast mixture. Near the edges of the eruption column (outer shear layer, as discussed earlier) the density is low compared to the density of the ambient air. Thus entrainment is increased resulting in the increase of its width.

The characteristics of the plume depend upon factors like wind speed, atmospheric stratification, humidity, etc. One of the dangerous constituent of many volcanic eruptions

is SO$_2$, which reduces the amount of ozone in the atmosphere because of its reactive nature, as shown in Eqn. 1.5.

$$S0_2 + O_3 \rightarrow SO_3 \tag{1.5}$$

If the background flow is windy, the huge fraction of gases wash out in the direction of the wind. In the absence of the wind, gravitational settling of these gases is observed (Meisser, 2011). If the pyroclastic plume reaches upper atmosphere, the plume content i.e., (ashes, gases) can spread to a wide area over the planet, leading to potentially disastrous events.

As an example of the destructive nature of the volcanoes, the lateral blast of Mount St. Helens (1980), contained a pyroclastic mass of 3.25 x 10^{11} kg at a temperature of 600°K which spread up to 50 – 300 kms with an energy content equivalent to 3.7 mega tonnes of TNT (Myagkov, 1998).

Volcanic flows are not axisymmetric in nature, and when the volume flux of volcanic eruption vary with time then a flow field similar to an unsteady jet is observed in the eruption column. These conditions arise when the volume flux variations with respect to time are of order $1/N$, N being the atmospheric buoyancy frequency (Chojnicki et al., 2015). The value of N is approximately 0.01 seconds. Most of the current volcanic models, however, are based upon simple turbulent models of steady jets, which cannot accurately predict the actual scenario, i.e., the unsteady nature of the volcanic plumes. When the material from volcanic vent ceases, the eruption ends but short-lived volcanic plumes continue to ascend for long times after the discharge stops. Most commonly, three types of volcanic
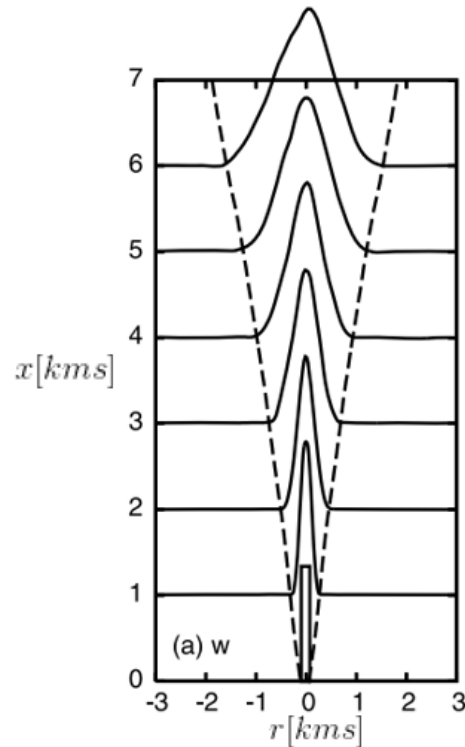
Figure 1.21.Temporal averaged radial profiles of (a) vertical velocity corresponding mass flux at different heights. *x*-axis and *y*-axis (radial distance r[kms] and vertical distance x[kms])are shown respectively. As summarized from Suzuki & Koyaguchi (2010).

eruptions are observed: 1. Strombolian, 2. Plinian, 3. Vulcanian (see Fig. 1.22). Volcanic

plumes can ascend up to an altitudes of 10 kms above sea level and last for tens of hours.

Strombolian eruptions last for tens of seconds and rise up to an altitude of 5 kms from the

volcanic vent. Vulcanian eruptions rise up to 5 – 20 kms and last from tens of seconds to

tens of minutes. Similar to a cough puff, as the volcanic plume ascends into the atmosphere

then turbulent eddies at the edge of the plume draw in ambient air into the jet. Mixing of

the material in the plume and ambient air is observed during this entrainment process. A

decrease in initial momentum is seen, and the forward momentum from buoyancy act as a

force thereby increasing the height of the plume. In the absence of these buoyant forces, the plume settles under the effect of gravity once its initial momentum diminishes.
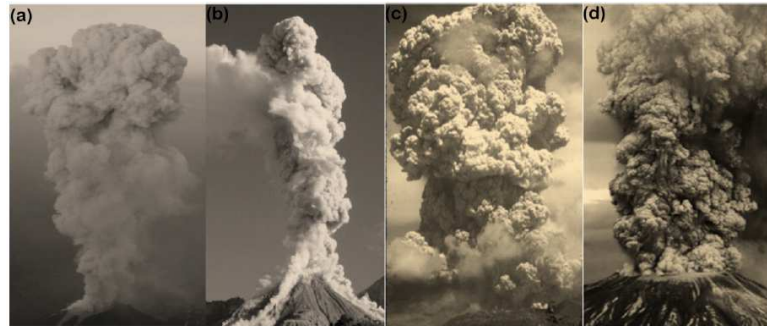
Figure 1.22.Different ranges of volcanic eruptions are shown. a) pyroclastic material rising < 1 kilometer above sea level at Santiaguito Volcano, Guatemala. b) cylinders of material rising < 5 kilometer above sea level at Santiaguito Volcano. c) large cylinders of material rising > 5 kilometers above sea level d) conical columns of material rising > 25 km at Mount St. Helens, U.S.A. As taken from Chojnicki et al. (2014).

Insight into the length and time scales of plume assist in understanding the dilution of initial momentum, buoyant nature of the plume and the entrainment. Chojnicki et al. (2014) conducted an experiment where time-dependent discharges were studied. Pressurized water was injected into a still water tank at $Re = 10^3 – 10^5$ based on exit velocity, which corresponds to smaller volcanic plumes. It was observed that once the initial momentum starts to dilute the flow, it is unstable and breaks down into large-scale eddies with an increase in downstream axial location with small-scale structures near the source. During the process of break down, the entrainment of the ambient fluid into the flow field is also seen. Two phases of the flow are observed: 1) A phase where the evolution of the flow depends on the source and 2) a phase where the source has no control over the dynamics of the flow (Chojnicki et al., 2015). This process is similar to what Bourouiba et al. (2014) explained, i.e., the eruption column is dominated by the initial momentum from the source

and after a certain downstream axial location then the eruption cloud is dominated by the effect of buoyancy.
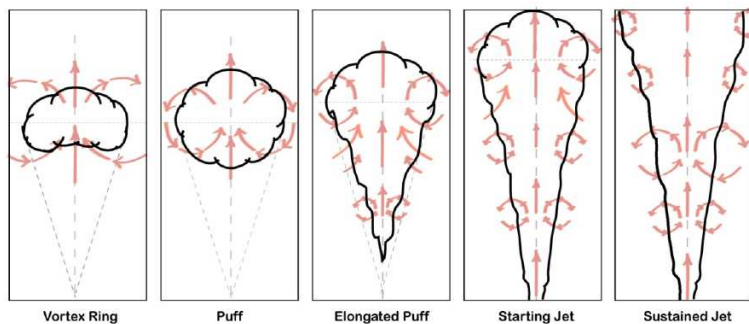
Figure 1.23.Schematic of large and small eddies are seen in different kind of flows. As taken from Chojnicki et al. (2014).
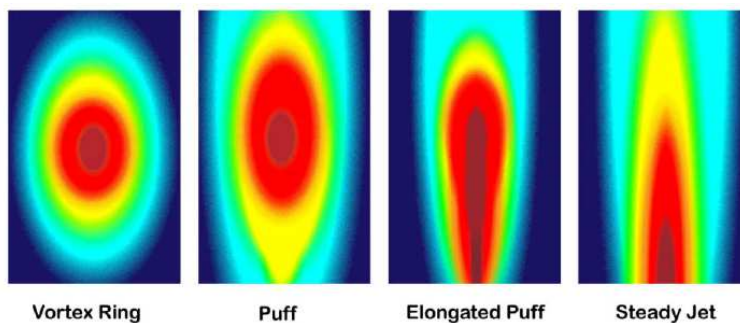
Figure 1.24.Time averaged Vertical velocity distributions of turbulent flows where jet moves from bottom to top of the figure. As taken from Ghaem-Maghami & Johari (2007).

1.6 Current Focus

Several types of jet flows namely steady turbulent jets, puffs, vortex rings are shown in Fig. 1.23. Steady turbulent jets have a continuous source of momentum, and as they move away from the source the high momentum jet mixes with the low-momentum ambient air and increases the width (radius) of the jet. Velocities near the source and center of the flow are high, as shown in Fig. 1.24. A decrease in centerline velocity is observed with an increase in downstream axial location, which in-turn depends on the initial momentum supplied to the jet or the dilution rate of the momentum by entrainment. Large coherent structures dominate the flow motion in the near-field and transition field for the steady case (see Fig. 1.23). These are the regions where the fluid flow follows a path rather than spreading out in random directions, and these effects dominate dynamics of the flow in this region, i.e., entrainment of fluid reducing momentum. Similarly, in the case of vortex rings and puffs, large flow structures dictate the dynamics of flow. Puffs and rings are a special cases of a steady jet, i.e., these are generated by the instantaneous release of momentum. Small volume injections create vortex rings, and for intermediate volume injections puffs can be observed. Structurally, the absence of a tail is observed for a ring (Ghaem-Maghami & Johari, 2007) when compared to the puffs (see Fig. 1.24). Investigation of far-field velocity distributions for rings and puffs was done by Ghaem-Maghami & Johari (2007), as shown in Fig. 1.24, and velocities were found to be high in the center of the puff or ring but decreased radially away from the center. Further, Ghaem-Maghami & Johari (2007) observed that above the core the fluid moves radially outward and below the core the fluid

is brought into the structure. In Fig. 1.23, the core location is shown by the centerline and above the line the flow is directed away, and below the line it is directed into the core.

Much of the work on turbulent puffs has focused on single ejection events. However in reality as in the case of human coughs, volcanoes or fuel injection multiple ejection events are ejected into ambient with some time separation.

The objective of the present study is to determine if there is any difference in the flow evolution of a single puff and dual puff. If such a difference exists, how does the flow field vary with time separation Δ_p between the two consecutive puffs

In the present chapter an introduction and background motivating the present study is presented. Chapter 2 presents the experimental framework built to investigate this problem. Chapter 3 presents the results and discussion while chapter 4 summarizes the conclusions while providing direction for future work.

2. Description of the Experiment

This chapter presents the details of the experimental facility, measurement techniques used for mean velocity measurements as well as the details of the flow visualizations carried out.

2.1   Experimental Facility
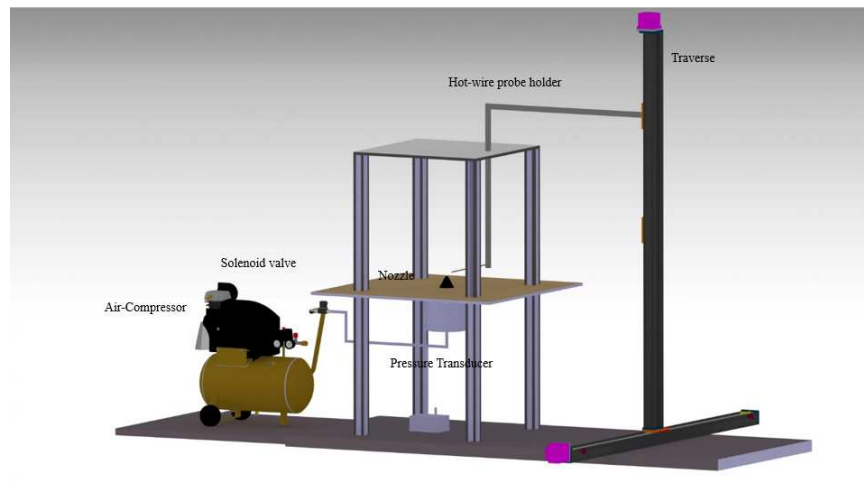
Figure 2.1.Schematic of the experimental setup showing the salient features.

A schematic of the experimental setup is shown in Fig. 2.1. A nozzle of diameter 0.196 in was connected to one end of a cylindrical settling chamber. The other end of the chamber was connected to a compressor which supplies pressurized air. This pressurized air passes through a solenoid proportional valve. An input pulse controls the opening/closing the valve for the specified time interval Δ_p s. The cylindrical chamber has honeycomb flow straighteners, which straightened the incoming flow before it enters the nozzle. The puffs

exiting the nozzle is enclosed in an acrylic box of dimensions 24×24 in^2 to minimize interference with external air currents.

All mean velocity measurements were carried out using hot-wire anemometry operating in constant temperature mode. The sensing element of the hot-wire was a wollaston wire of $\approx$ 2.5 microns in diameter. The hot wire sensor was firmly mounted onto an aluminum strut, and traversed through the flow field using a computer controlled traverse system. The resolution of the traverse system was $\approx$ 6.35 micron per step. All measurements were acquired using a data acquisition board (DAQ) in conjunction with a computer. The DAQ board that was used was a Data Translation DT-9836 16-bit Analog/Digital system which has a voltage range of $\pm$ 10V and was controlled using MATLAB® scripts.

The solenoid valve used was an Omega FSV10 Series electronic proportioning solenoid valve. A pressure regulator was used at the compressor exit to set the back pressure on the solenoid valve. The FSV10 Series uses a DC signal as an input control to open or close the valve proportionally. This voltage is generated and supplied using the Analog output channel of the DAQ board. The input is a square wave where the max voltage is proportional to the extent the valve is opened and the period of the wave controls the valve open duration.

A differential pressure transducer measured the stagnation pressure in the settling chamber. This transducer outputs a voltage proportional to the differential pressure (difference between the stagnation pressure and the atmospheric pressure) which is recorded by the DAQ board. A National Instruments thermocouple was used to measure the atmospheric temperature, which was recorded via USB.

2.2   Flow Visualization

All flow visualizations were carried out using a Nd:YAG laser designed for high speed flow analyses. The light scattered by the particles is captured by a high speed camera to measure the spatial resolution. A Phantom v641 with a resolution of 2560x1600 with 500 frames per second was used for this purpose. The camera was placed normal to the light sheet. Theatrical particles were used as seeding particles.

2.3   Hot Wire Calibration

The hot wire anemometer was calibrated using the jet while varying its exit velocity from 0 to approximately 6 ms^{-1}. The pressure difference i.e., between the ambient and stagnation pressure in the jet chamber was used to calculate the jet exit velocity using Bernoulli's equation. The sampling period was set to 30s, and the mean voltage was measured as a function of the flow velocity. A curve fit (4th order polynomial) was used to convert the measured voltage to velocity. A typical calibration curve obtained is shown in Fig. 2.2.

2.4   Uncertainty and Measurement Error

This section summarizes the different sources of error in the experimental setup and the measurements. Though the solenoid input pulse and the back pressure on the solenoid was set to be a constant, there was a small periodic fluctuation in the input pressure. This is due to the air compressor automatically refilling as the compressor tank gets emptied.
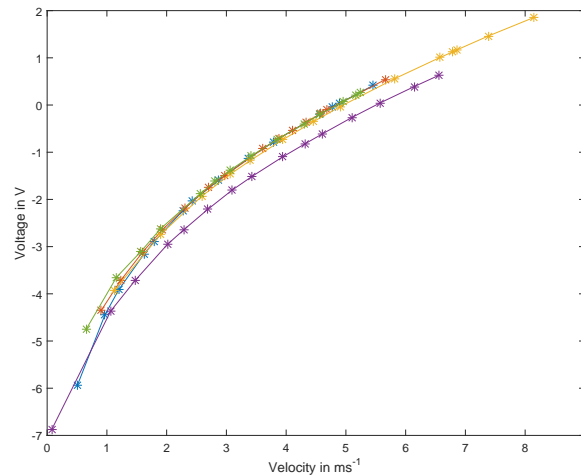
Figure 2.2.Calibration curve of the hot-wire probe. x – ordinate is the velocity in ms^{-1}, y – ordinate is the voltage in volts respectively.

Due to the low velocities being measured the hot-wire was also particularly sensitive to ambient vibration in the laboratory. The temperature drift in the hot-wire sensor is another significant source of error. This is minimized by calibrating the hot-wire everyday. The maximum variation in the calibrations at 0.8 ms^{-1} was 0.1563 ms^{-1} and at 3.42 ms^{-1} the corresponding variation was 0.0517 ms^{-1} indicating greater uncertainty at lower velocities. To get an estimate of the repeatability of the input pressure pulse the maximum pressure in the settling chamber was considered. The maximum voltage from the pressure transducer was tracked over each set of measurement and were tabulated in Appendix A. The standard deviation of this maximum voltage was at most 3.5%, showing good repeatability of a pulse.

2.5   Measurement Details

Mean velocity measurements about the jet centreline were carried out at four axial locations (x/d = 1, 5, 10, 15) spanning the width (radial) of the jet, as shown in Fig. 2.3. At each spatial location, the velocity field of forty sets of puffs (single and double) were recorded. These measurements were then ensemble averaged over a single or double puff (as the case may be) to yield a mean velocity field. The DAQ board recorded the velocity fields as well as the solenoid input pulse. Sample solenoid input pulses along with the velocity at the jet exit (x/d = 1) for the both a single and double puff are shown in Fig. 2.4 (single puff) and Fig. 2.5 (double puff).
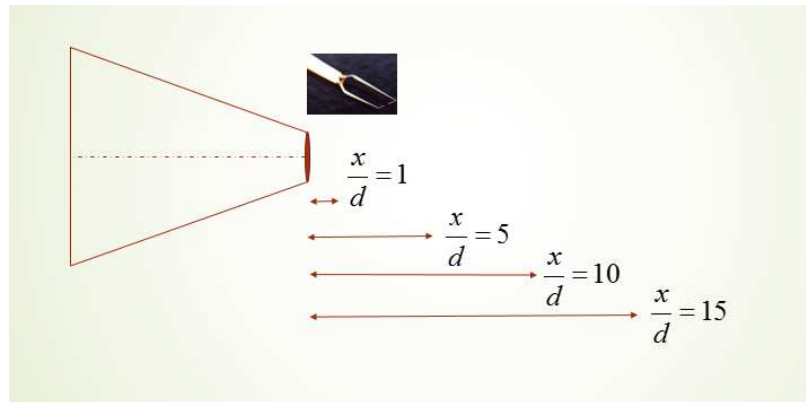
Figure 2.3.Velocity measurements at different axial location away from the nozzle.
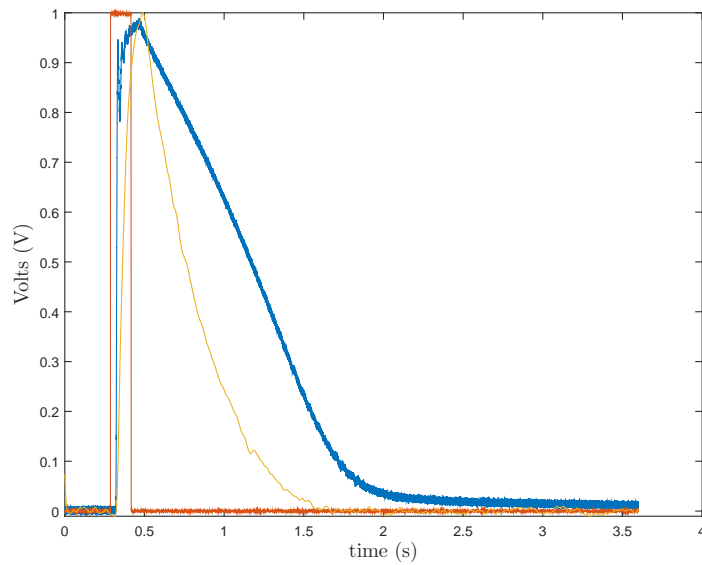
Figure 2.4.Two-dimensional plot of the hot-wire voltage signal, TTL signal, pressure signal corresponding to single puff. x – axis is the time in s, y – ordinate is the voltage in volts respectively.
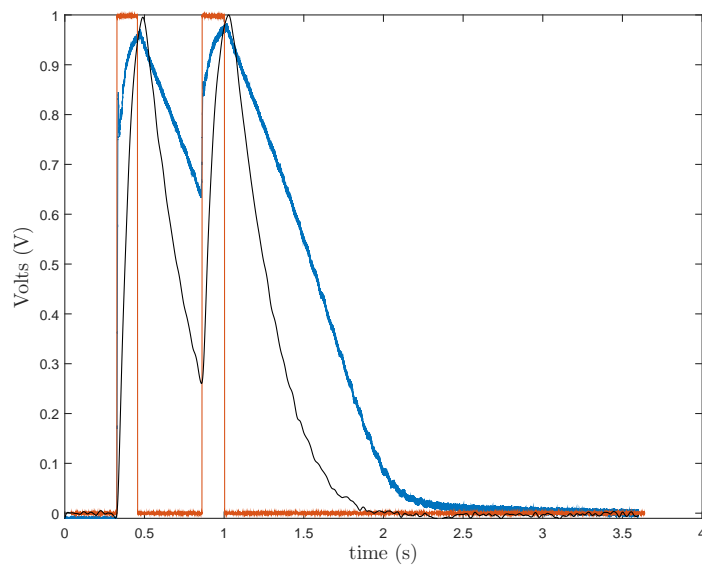
Figure 2.5.Two-dimensional plot of the hot-wire voltage signal, TTL signal, pressure signal corresponding to double puff. x – axis is the time in s, y-ordinate is the voltage in volts respectively.

3. Results and Discussion

Measurements were conducted using hot wire anemometry (HWA) to measure the mean velocity field of the puff flow field. Measurements were carried out at various radial and axial locations as described in the previous chapter. All the results in this chapter are presented in non-dimensional form using: x/d as the non-dimensional axial location, r/d as the non-dimensional radial location, V_j corresponds to the maximum axial velocity at $x/d =1$ and tV_j/d is the non-dimensional time.

Mean velocity flow measurements at several radial locations for the case of a single puff (SP) and four cases of double puffs (DP) were conducted at $x/d =1$, $x/d =5$, $x/d =10$ and $x/d =15$. The four different cases of double puffs were at varying $\Delta_p = 0.3$ s, 0.5 s, 0.7 s and 1.79 s. Here Δ_p is the time between the first and second puff. The hot-wire measurements were averaged over 30 – 40 puffs at each measurement position. The jet was ensured to be puffing in a repeatable manner while measuring these mean velocity fields. The data is primarily presented using three-dimensional line plots and two-dimensional contour plots. At each axial location the time record was offset such that the start of the puff was always at zero. Mean velocity measurements were also carried out with a steady jet (SJ), i.e. a jet with constant exit velocity. The single puff is referred to as SP, the double puff is referred to as DP and the steady jet is referred to as SJ.

The cases studied are summarized in Table. 3.1. The symbols used in line plots are also shown in the table along with the corresponding Δ_p. The Reynolds number was calculated to be nominally $Re \approx 1,350$ where

$$Re = \frac{\rho V_{avg} d}{\mu} \tag{3.1}$$

ρ and μ were calculated using the ambient temperature and pressure using the ideal gas law and Sutherlands law, d is the diameter of the nozzle and V_{avg} is the mean of maximum velocities for cases a – f at $x/d = 1$.

Table 3.1.: Table for cases a-f showing maximum exit velocity and Reynolds Number

Label	Type	Δ_p(s)	V_j (ms^{-1})	Re	Plot symbol
a	SJ		4.3	1373	○
b	SP	0	3.7	1184	×
c	DP	0.3	4.3	1385	△
d	DP	0.5	4.5	1431	□
e	DP	0.7	4.5	1443	▽
f	DP	1.79	4.2	1349	+

All the flow visualizations discussed in the following sections have $Re \approx 1675$ with an exit velocity of 5.5 ms^{-1}. The flow visualization of the baseline steady jet is shown in Fig.3.1. As the flow evolves downstream, at axial location approximately $x/d = 5$, Kelvin Helmholtz instability modes are seen with increasing downstream distance secondary instability modes are seen which breaks down the flow structure into fully blow turbulence at approximately $x/d = 10$.
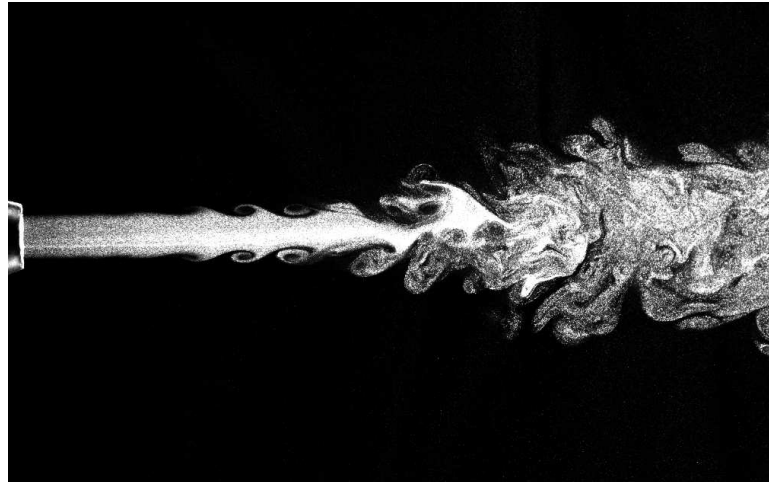
Figure 3.1. Flow visualization of steady jet at t = 0.468s

3.1 Single Puff, SP

Flow visualizations of a single puff exiting the nozzle are shown in figures 3.2(a) – 3.2(d). The starting vortex corresponding to the single puff is clearly evident at x/d = 1 (t = 0.298s) and with increase in downstream distance the size of the starting vortex is seen to increase. A series of secondary vortices are seen to follow the initial starting vortex. These vortices are due to the Kelvin Helmholtz instability. At x/d = 15 (t = 0.374s) these vortices are seen to breakdown and the flow becomes fully turbulent.

All the axes of three-dimensional line plots in this chapter are normalized as follows: the x-axis is tV_j/d which is the normalized time, the y-axis is r/d which is the normalized radial location and the z-axis is V/V_j which is the normalized velocity. The axes for the velocity magnitude surface contour plots are as follows: the x-axis is the normalized radial location r/d, the y-axis is the normalized time tV_j/d and the color contours are contours of normalized velocity V/V_j.

Mean velocity fields at various radial locations with increasing downstream distance are shown in Fig.3.3. As the puff exits the nozzle a shear layer is generated between the fluid injected and the ambient air. This shear layer is unstable and rolls back on itself creating a starting vortex. The starting vortex is the largest coherent structure present in this flow, and it is likely that this dominates the flow evolution. It is evident from Fig.3.3 that at $tV_j/d \approx$ 20, a peak in the non-dimensional velocity V/V_j is seen which corresponds to the starting vortex. The potential core is the region where the centerline velocity remains constant and is nearly equal to the velocity at the nozzle exit. The width of the potential core appears to be approximately between ($r/d \approx$ - 0.6 – 0.6) at this axial location. The radial distance at which the mean velocity becomes zero is the boundary of the spreading turbulent puff, which is the radial extent of the puff. Because of the uncertainty of measuring velocities $\leq$ 0.2 ms^{-1}, 20% of V_j is taken as a surrogate for the extent of the puff. This extent is shown as the red line in all the contour plots in Fig.3.4 and those that follow it.

With increasing downstream distance the interactions within the puff itself, as well as that between the puff and ambient fluid, dictate the dynamics of the evolving flow. Momentum dilution by turbulent mixing and entrainment increases the radial extent of the puff as seen in Fig.3.3(b) while the temporal extent in the pseudo contour plots is seen to decrease or remain the same. The velocity differences across the jet boundary with the ambient air leads to a Kelvin-Helmholtz instability.

As stated previously with an increase in downstream location the momentum starts to decrease, the reason being that the fluctuations causes the eddies to break up into smaller and smaller flow structures leading finally to their dissipation. Fig.3.3(c) show the mean

velocity profiles at axial location of x/d = 10. The radial extent of the single puff is seen to increase when compared with x/d = 5 and x/d = 1 as shown in Fig.3.3, which is also seen while inspecting the red line, which corresponds to $20\%V_j$. However, the temporal extent is seen to decrease or remain almost the same.

The axial location x/d = 15, corresponds to the downstream location where the flo in-stabilities breaks down the flow into fully blown turbulence as seen in Fig.3.2(d). A sudden drop in radial extent of the starting vortex is seen at this axial location indicating its dissi-pation. A decrease in temporal extent is also clearly evident as shown in fig.A.4(d). The flow field at this location is entirely turbulent which indicates an increase in entrainment and the associated momentum dilution.

(a)
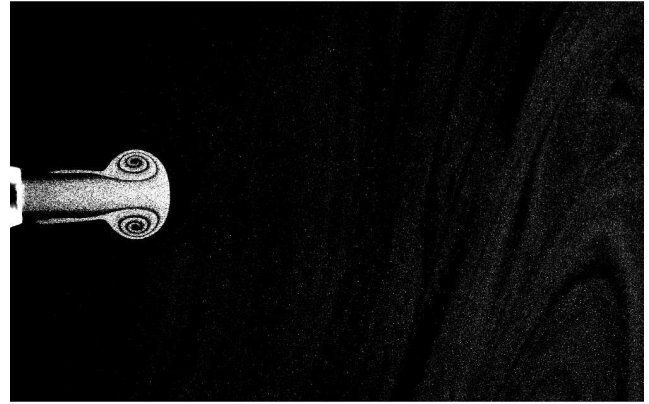
(b)
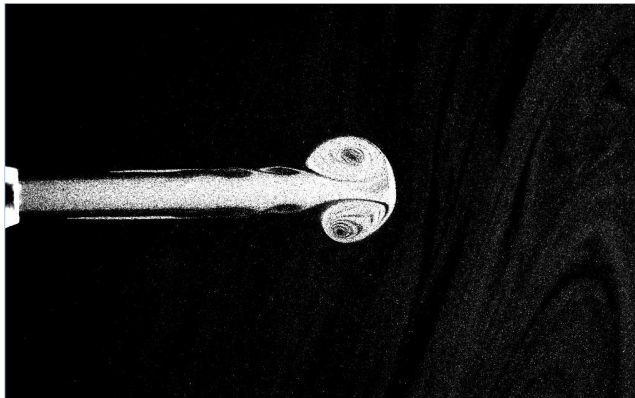
(c)

(d)

Figure 3.2. Flow visualization of a single puff with increasing downstream distance at *Re* = 1675 with respect to exit velocity (5.5 ms^{-1}) different time instances a) t = 0.298 s b) t = 0.318 s c) t = 0.326 s d) t = 0.374 s

Figure 3.3. Case b, Single Puff: Normalized axial velocities at axial locations from x/d = 1 to x/d = 15. x – ordinate is the non-dimensional radial location r/d, y – ordinate is the non-dimensional time tV_j/d , z – ordinate is the non dimensional velocity magnitude V/V_j respectively.

Figure 3.4. Case b, Single Puff: Pseudo contour plot of normalized axial velocities at axial locations from $x/d = 1$ to $x/d = 15$. x – ordinate is the non-dimensional radial location r/d, y – ordinate is the non-dimensional time tV_j/d. The color contours are the magnitudes of the non-dimensional velocity V/V_j.

3.2   Double Puff, DP, Δ_p = 0.5s

Flow visualization of a dual puff with Δ_p = 0.5 s is shown in Fig.3.5. The first puff is ejected into the flow at t = 0.314 s and with increasing downstream distance puff is seen to break down into turbulence x/d = 10. However, as the momentum of the first jet reduces it leaves a tail attached as shown in Fig. 3.5(c). As the second puff is injected into the flow domain the starting vortex corresponding to second puff is seen to interact with the tail of the first puff followed by transition into fully blow turbulence.

The second puff is injected into the flow domain when the first puff has a velocity which was 50% of the maximum velocity i.e. $V/V_j \approx$ 0.5 of the first puff. Similar to case b, case c, x/d = 1 for the dual puff with Δ_p = 0.5 s corresponds to the potential core of the puff.

The peak velocity of the starting vortex corresponding to the second puff is 50 % V/V_j of the first puff. From the three-dimensional line plot in Fig. 3.6 we observe that the velocity peak corresponding to the first puff is higher than the velocity peak corresponding to the second puff. The radial extent of the starting vortex corresponding to the first puff $\delta_{r_{V1}}$, is approximately 1.5 times that of that at x/d =1. The radial extent of the starting vortex $\delta_{r_{V2}}$, corresponding to the second puff is approximately 1.25 times of that at x/d = 1. Hence the radial extent of both the starting vortices is seen to increase in size with respect to x/d = 1. The temporal extent is seen to decrease or remain almost the same as shown in Fig.3.7 when compared with x/d = 1.

Mean velocity fields at axial location x/d = 10 is shown in Fig. 3.6 and Fig.3.7, the peak velocity of the starting vortex corresponding to the second puff was 50% V/V_j of the first

puff. The radial extent of the starting vortex corresponding to the first puff $\delta_{r_{V1}}$, was found to be approximately 2.1 times the radial extent of that at $x/d = 1$ and approximately 1.38 times of that at $x/d = 5$. The radial extent of starting vortex corresponding to the second puff $\delta_{r_{V2}}$, is found to be approximately 1.6 times of that at $x/d = 1$ and approximately 1.18 times of that at $x/d = 5$. Hence the radial extent of both the starting vortices is seen to increase in size with respect to $x/d = 1$ and $x/d = 5$. However, the temporal extent is seen to decrease or remain almost the same when compared with $x/d = 1$ and $x/d = 5$.

Considering the axial location at $x/d = 15$ as shown in Fig. 3.6 the radial extent of the starting vortex corresponding to the first puff $\delta_{r_{V1}}$, is approximately 2.6 times of that at $x/d = 1$ and approximately 1.77 times of that at $x/d = 5$ whereas it is approximately 1.28 times of that at $x/d = 10$. The radial extent of the starting vortex corresponding to the second puff $\delta_{r_{V2}}$, is approximately 1.83 times of that at at $x/d = 1$ and approximately 1.37 times of that at $x/d = 5$ whereas it is approximately 1.15 times of that at $x/d = 10$. Increment in radial extent indicates the increase in entrainment followed by the breaking down the puff and its dissipation.

Dual puff with $\Delta_p = 0.3$ s, 0.7 s showed similar behavior to $\Delta_p = 0.5$ s as shown in the Appendix.
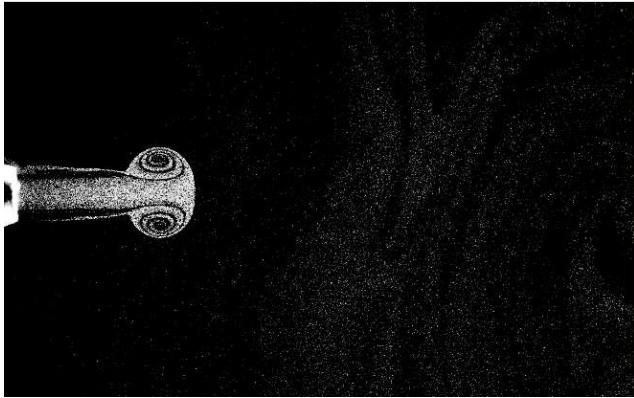
(a)
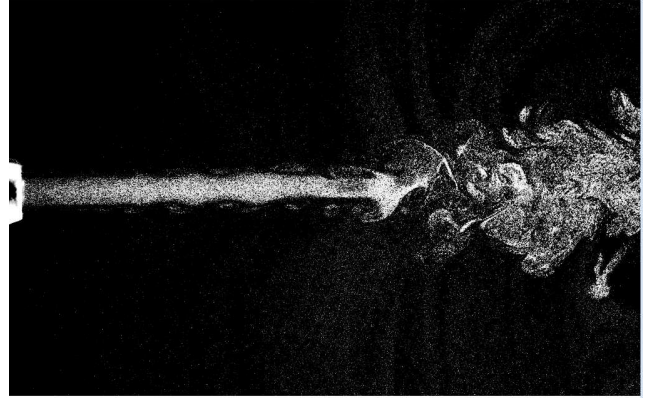
(b)

(c)

(d)

Figure 3.5. Flow visualization of double puff (Δ_p = 0.5 s) with increasing downstream distance at Re = 1675 with respect to exit velocity (5.5 ms^{-1}) different time instances a) t = 0.314 s b) t = 0.37 s c) t = 0.808 s d) t = 0.99 s
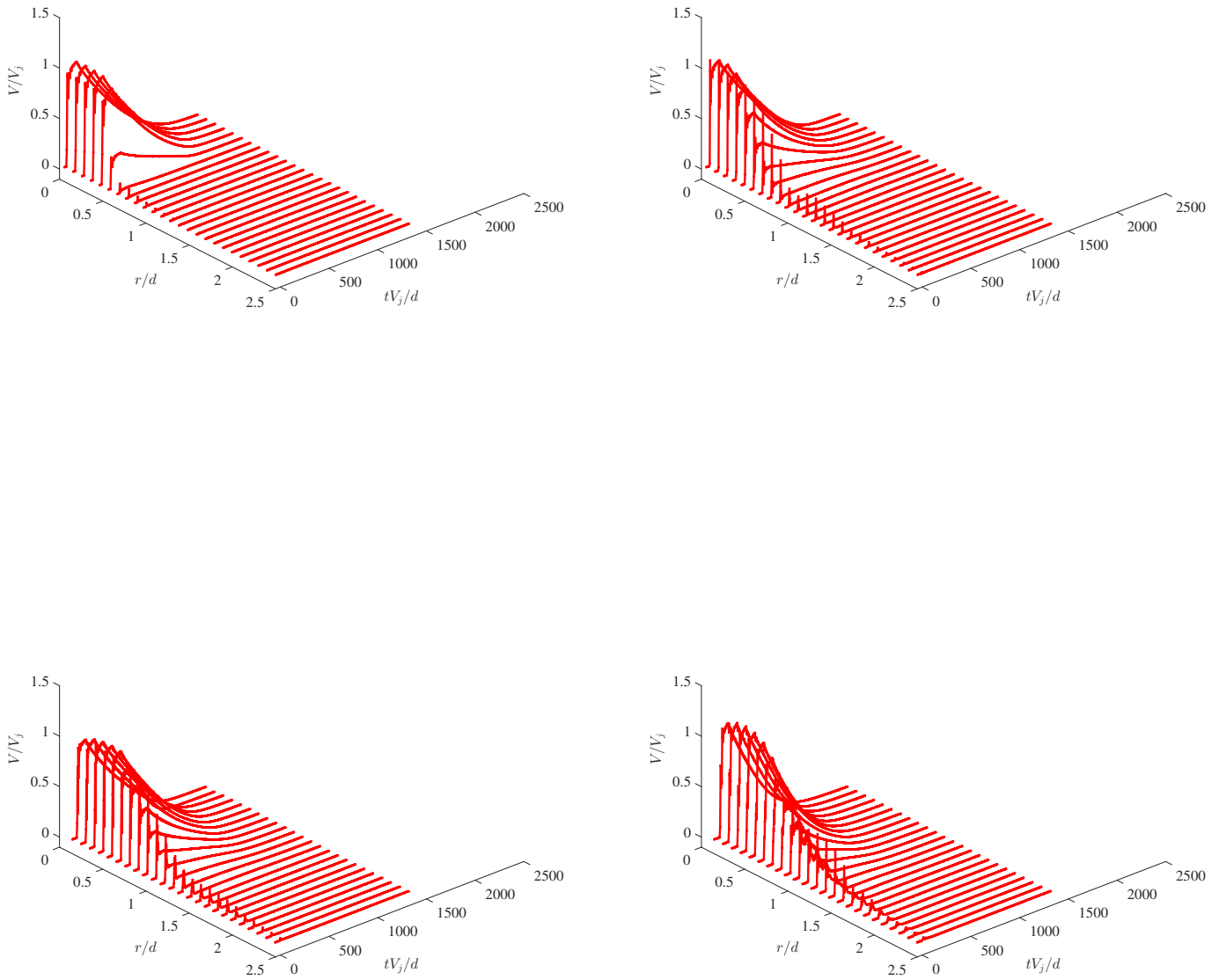
Figure 3.6. Case d (Double puff, Δ_p = 0.5s): Normalized axial velocities at axial locations from x/d = 1 to x/d = 15. x – ordinate is the non-dimensional radial location r/d, y – ordinate is the non-dimensional time tV_j/d , z – ordinate is the non dime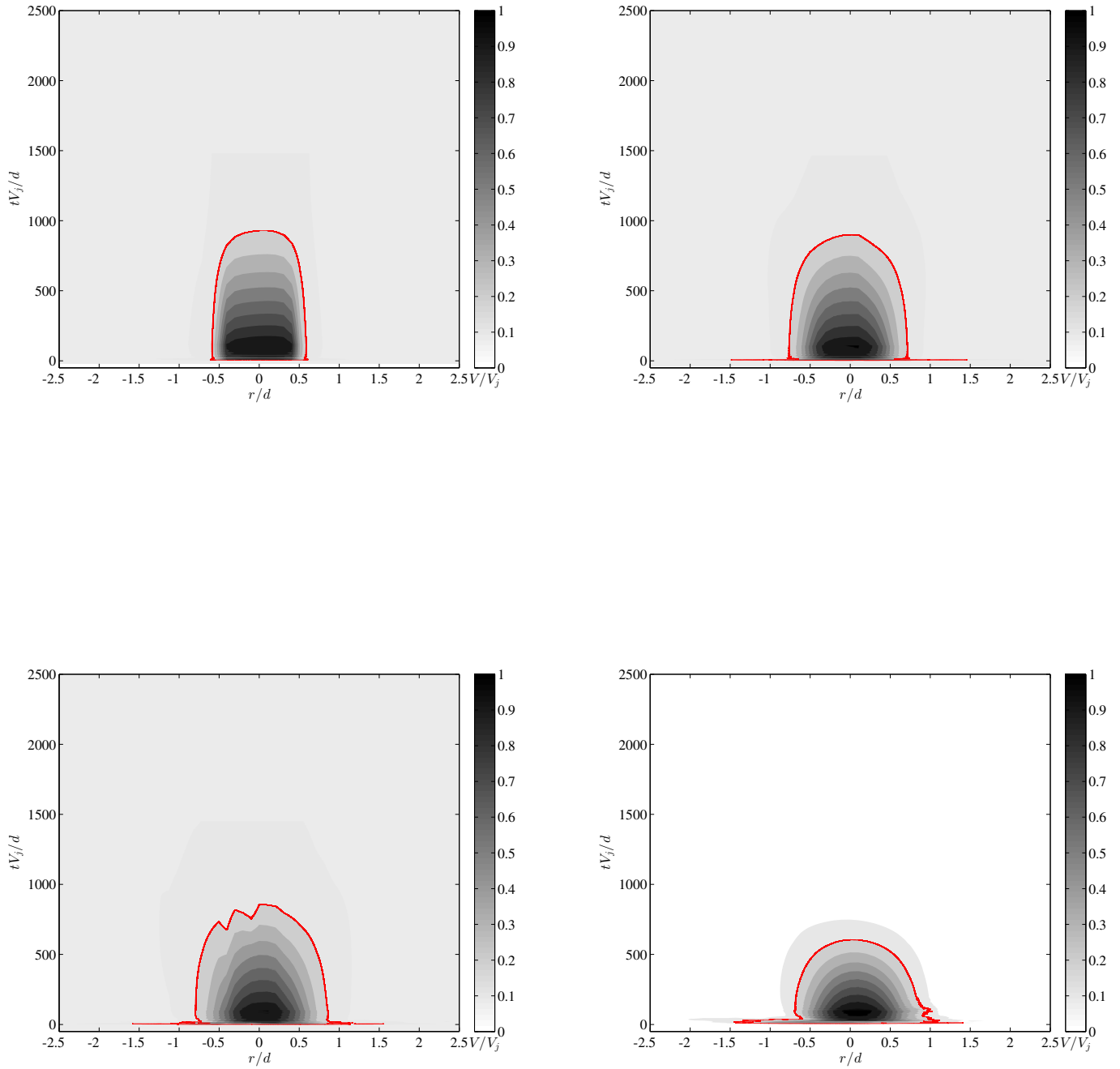nsional velocity magnitude V/V_j respectively. The color contours are the magnitudes of the non-dimensional velocity V/V_j..

Figure 3.7. Case d (Double puff, $\Delta_p = 0.5$s): Pseudo contour plot of normalized axial velocities at axial locations from $x/d = 1$ to $x/d = 15$. x – ordinate is the non-dimensional radial location r/d, y – ordinate is the non-dimensional time tV_j/d. The color contours are the magnitudes of the non-dimensional velocity V/V_j.

3.3   Double Puff, DP, Δ_p = 1.79s

For Case f the second puff exits the nozzle 1.79 s after the first puff as shown in Fig-ures. 3.9 and Fig.3.10. The flow visualization of double puff with Δ_p = 1.79s is shown in Fig.3.8. The first puff (Fig.3.8(a)) behaves as a single puff and as it translates downstream, a tail is seen before the second puff is injected into the flow field. Interaction between the tail and the second puff is observed (Fig.3.8(c)). With increase in downstream distance the flow breaks down into fully blown turbulence at x/d = 10.

The temporal extent for both the puffs are nominally equal i.e. $(tV_j/d \approx 20$ to $tV_j/d \approx 1000)$ for the first puff and $(tV_j/d \approx 1500$ to $tV_j/d \approx 2500)$ for second puff. Each of these puffs individually have a velocity field similar to the single puff (SP) velocity profile as seen in Fig. 3.9.

At x/d = 5, the radial extent of the starting vortex corresponding to the first puff δ_{rV1}, was approximately 2.6 times of that at x/d =1 . Since these are like two distinct single puffs the radial extent δ_{rV2}, is same as δ_{rV1}. The radial extent is seen to increase with respect to previous axial location and the size of the starting vortex is comparatively bigger in size than that of at x/d = 1.

The radial extent is seen to increase in size at the axial location x/d = 10 than that observed at x/d = 1 and x/d = 5. At x/d = 10, the peak velocity of the starting vortex corresponding to the second puff was 20% V/V_j of the first puff. The radial extent of the starting vortex corresponding to the first puff δ_{rV1}, is found to be approximately twice that at x/d = 1 and approximately 0.96 times of that at x/d = 5. This behavior is observed to

be the same for all the Cases (≤ 0.7 s) for the first puff except for case d. The radial extent of starting vortex corresponding to the second puff $\delta_{r_{V2}}$, is found to be approximately 2.29 times of that at $x/d = 1$ and approximately 1.35 times of that at $x/d = 5$.

However, there is a sudden drop in the radial extent of the mean velocity field at $x/d = 15$ which indicates the dissipation of the puff due to the flow instability and increment in entrainment of ambient air disrupting the evolving flow structure. The radial extent of the starting vortex corresponding to the first puff $\delta_{r_{V1}}$, decreases approximately to 2.5 times the radial extent of that at $x/d = 1$ and decreases approximately 0.96 times of that at $x/d = 5$ and approximately 0.90 times of that at $x/d = 10$.
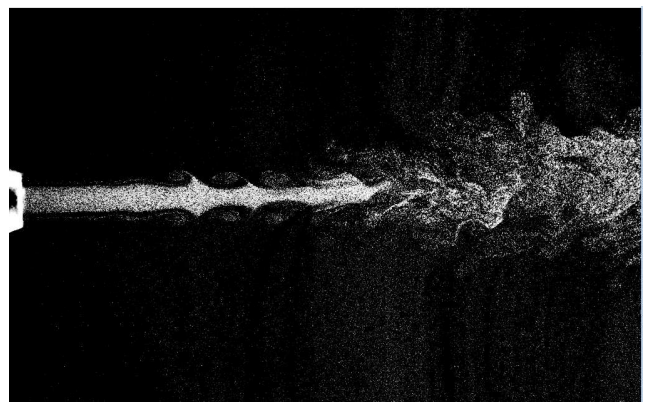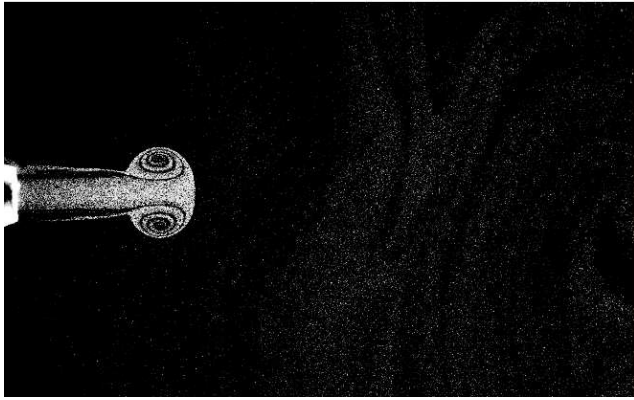
(a)
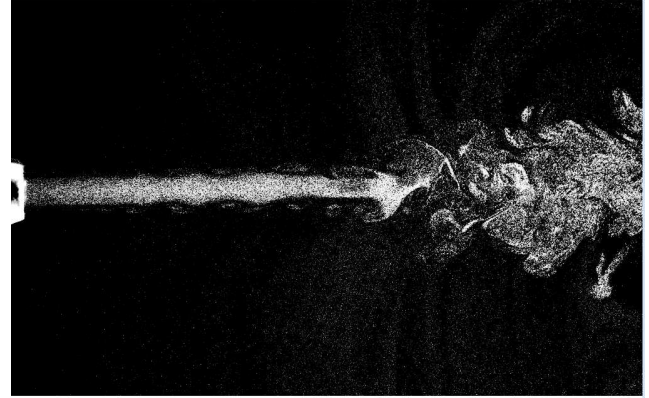
(b)
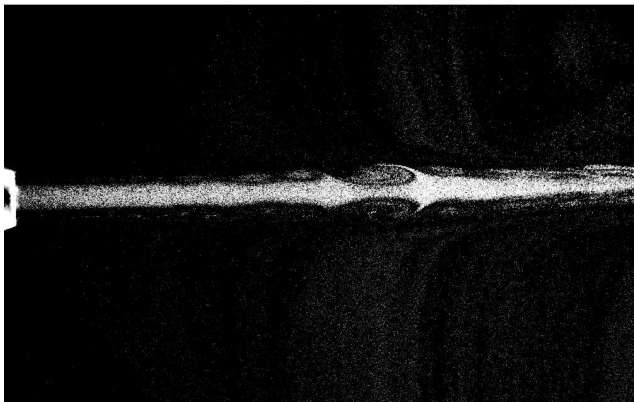
(c)
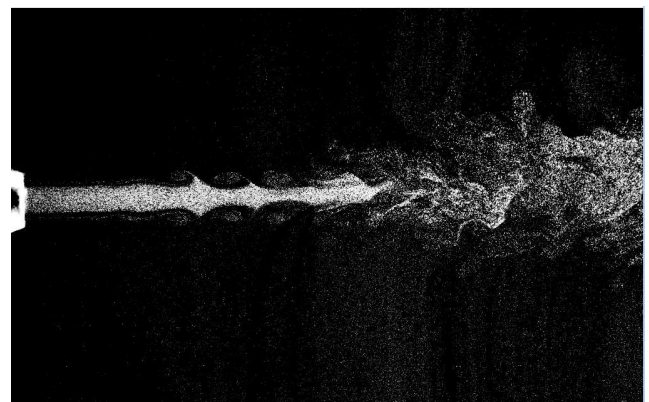
(d)

Figure 3.8. Flow visualization of double puff (Δ_p = 1.79 s) with increasing downstream distance at Re = 1675 with respect to exit velocity (5.5 ms^{-1}) different time instances a) t = 0.316 s b) t = 0.39 s c) t = 2.11 s d) t = 2.21 s
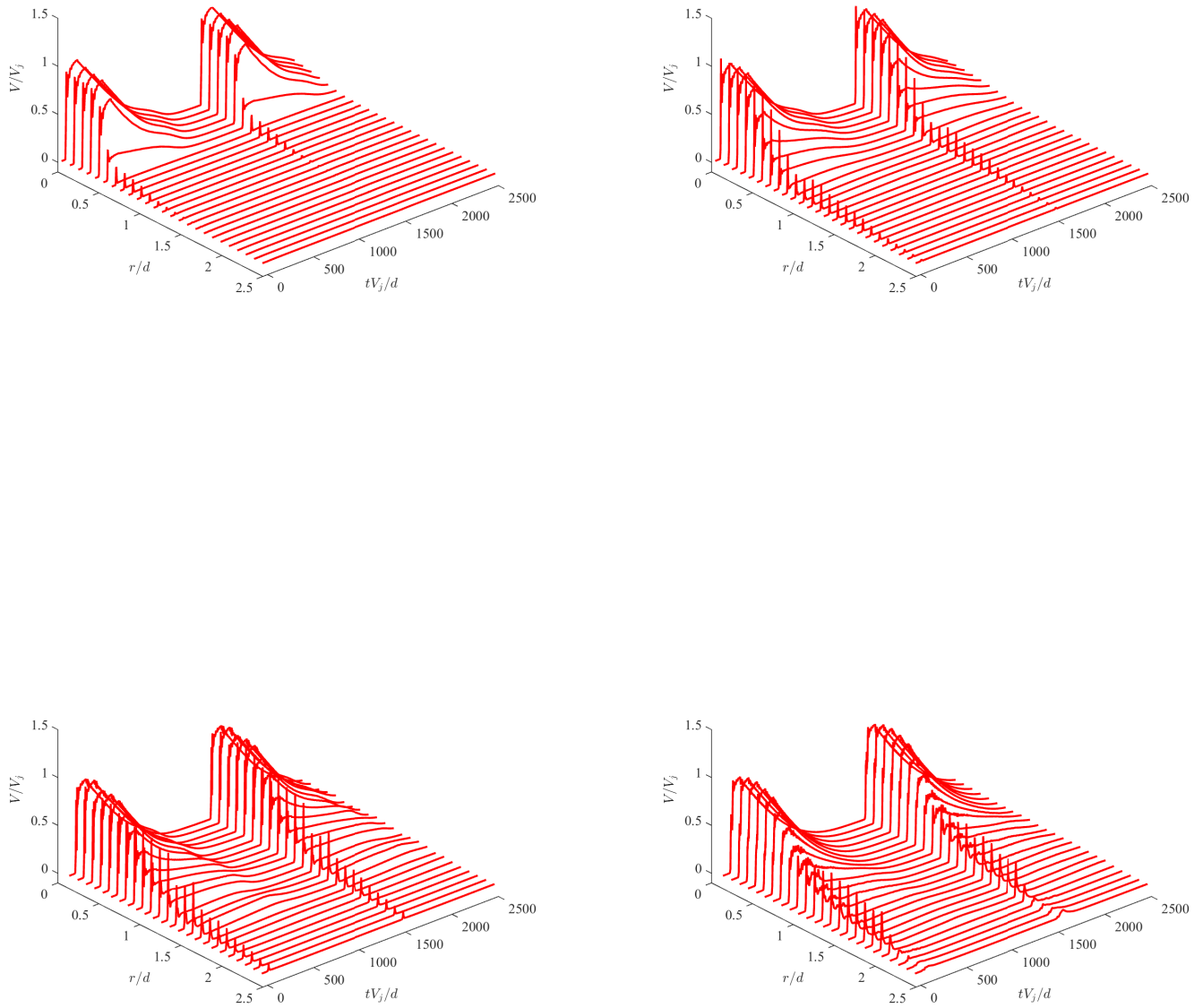
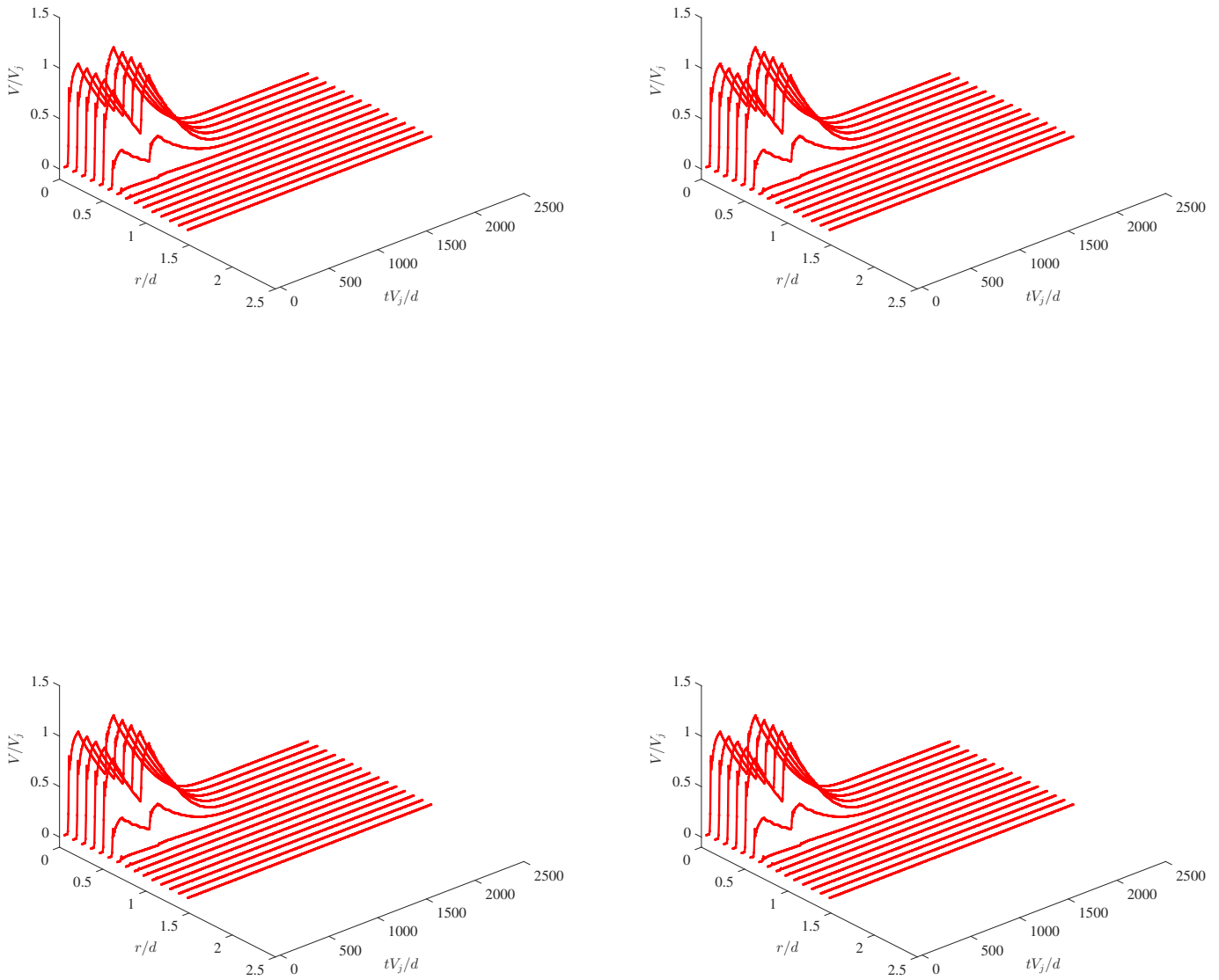Figure 3.9. Case e (Double puff, Δ_p = 1.79s): Normalized axial velocities at axial locations from x/d = 1 to x/d = 15. x – ordinate is the non-dimensional radial location r/d, y – ordinate is the non-dimensional time tV_j/d , z – ordinate is the non dimensional velocity magnitude V/V_j respectively. The color contours are the magnitudes of the non-dimensional velocity V/V_j.
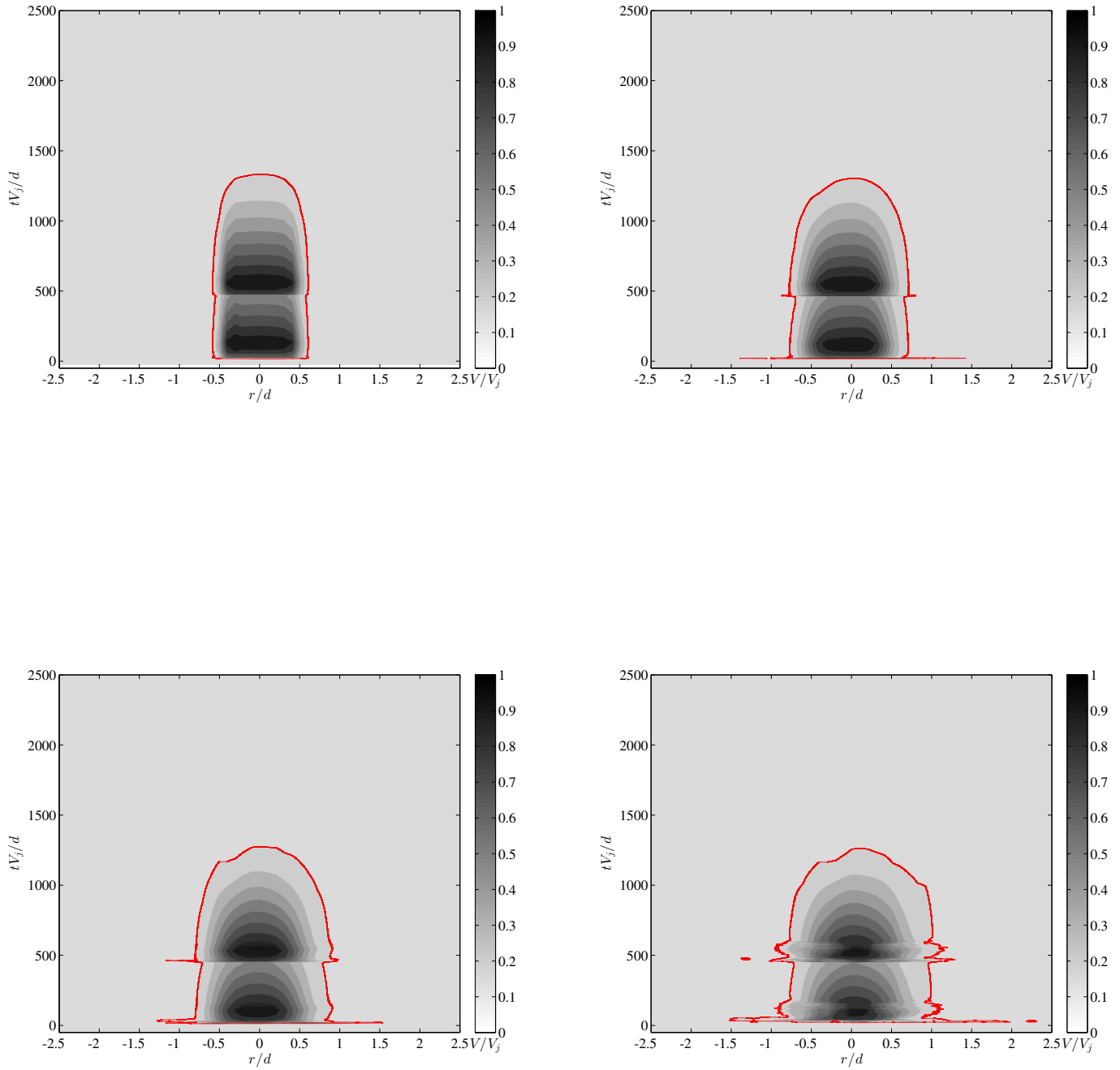
c
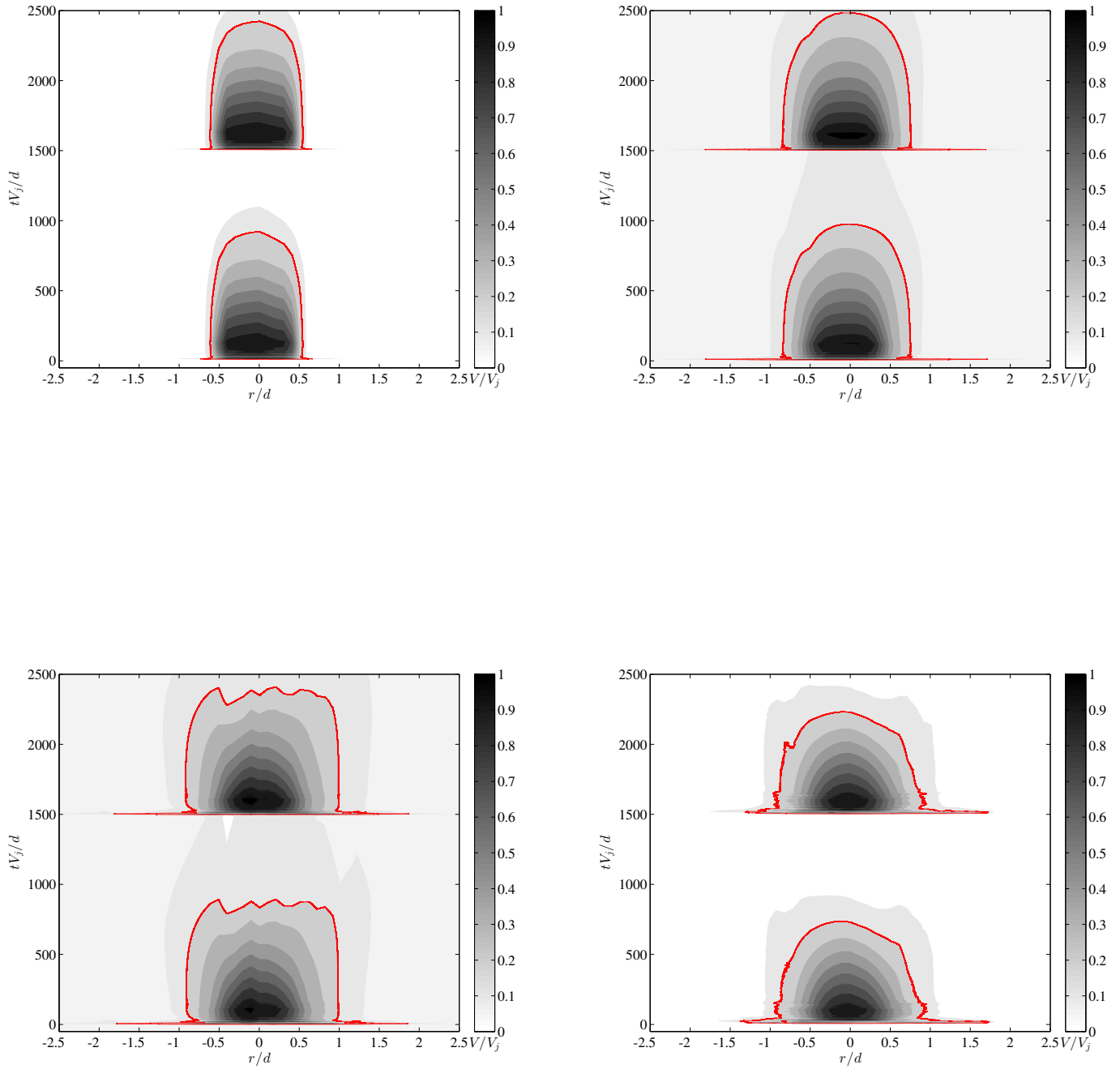
Figure 3.10. Case f (Double puff, $\Delta_p = 1.79$s): Pseudo contour plot of normalized axial velocities at axial locations from $x/d = 1$ to $x/d = 15$. x – ordinate is the non-dimensional radial location r/d, y – ordinate is the non-dimensional time tV_j/d. The color contours are the magnitudes of the non-dimensional velocity V/V_j.

3.4   Comparison with Steady Jet

Two-dimensional mean velocity profiles of a steady jet are compared with the two-dimensional maximum velocity profiles of all the cases of the puff as shown in Fig.3.11. At x/d = 1 radial extent of the mean velocity profile of a steady jet is approximately the same as the radial expansion of the maximum velocity profiles for all the puff cases. In contrast, for the axial locations of x/d = 5, x/d = 10 the radial extent of the two-dimensional mean velocity profile of steady jet is less than the radial expansion of the two-dimensional maximum velocity profile. However, at x/d = 15 radial extent both the mean and maximum velocity profiles are observed to remain approximately the same.
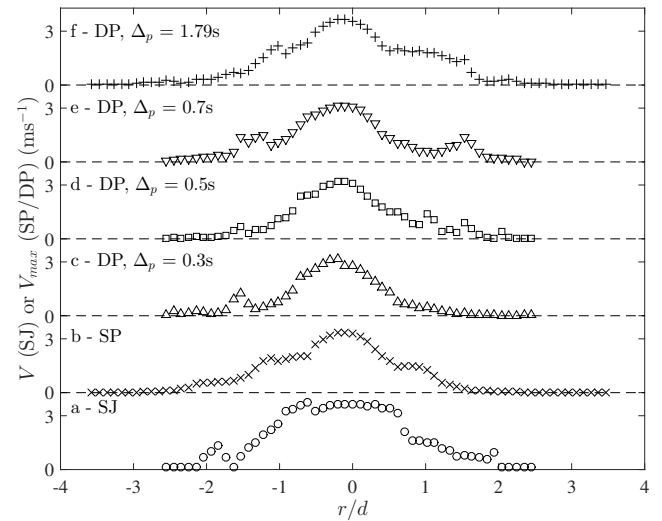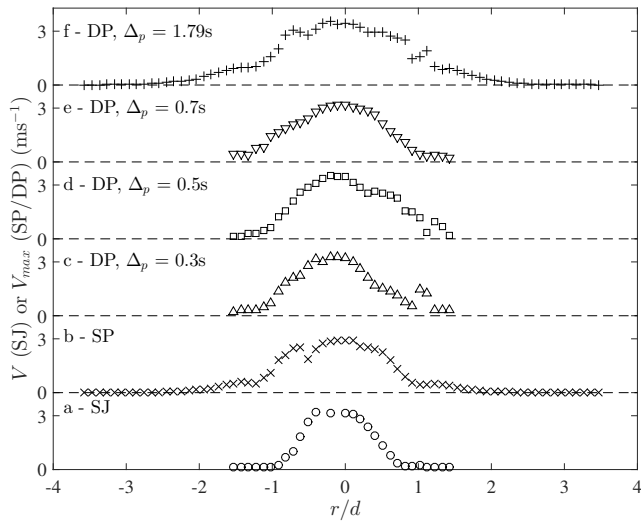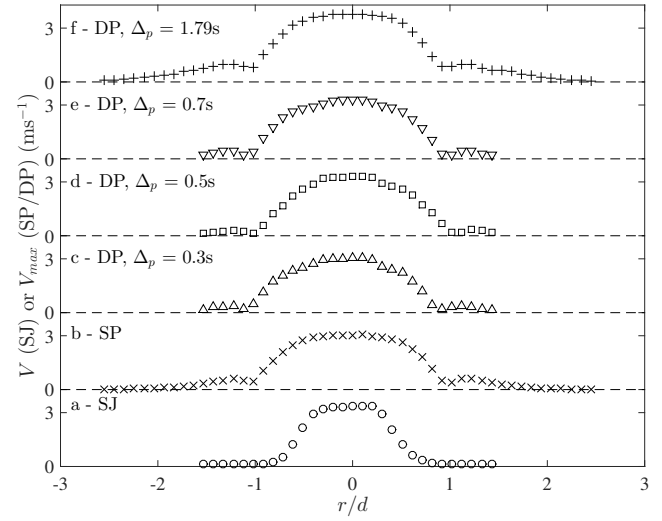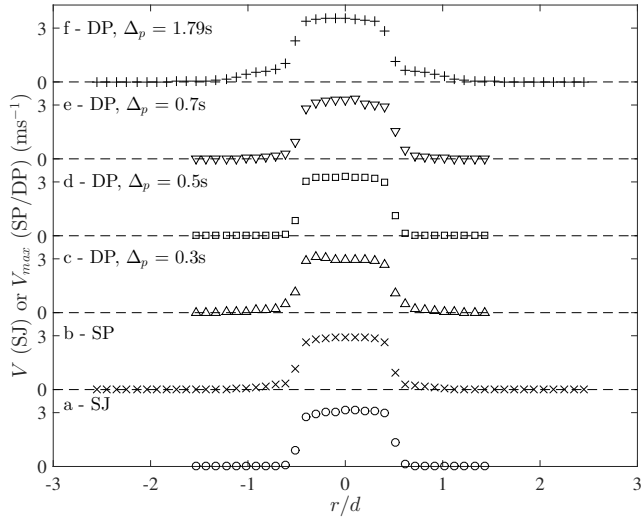
Figure 3.11. Mean velocity profile of the steady jet (case a) and maximum velocity profiles for cases b-f averaged over the entire puff cycle for the puffs. *x*-axis is the non-dimensional radial location *r/d*, *y*-axis is the non-dimensional velocity ms^{-1} for *x/d* =1, Legend: ∘ Case a: SJ, Steady jet, ×
Case b: SP, Single puff, △ Case c: DP, $\Delta_p \approx$ 0.3s, □ Case d: DP, $\Delta_p \approx$ 0.5s, ▽ Case e: DP, $\Delta_p \approx$ 0.7s, + case f: DP, $\Delta_p \approx$ 1.79s.

3.5 Radial Extents of Starting Vortices

As the starting vortices are the largest flow structure in the puff flow field, it is likely that their extents and evolution dictate the dynamics of the puff. Hence the radial extents of the starting vortices are summarized and discussed here. Figures. 3.12 and 3.13 summarizes the normalized extents of the starting vortices of the first puff and second puff corresponding to axial locations x/d = 1, 5, 10 and 15. It is noted that in Fig. 3.12, which corresponds to the starting vortex of the first puff $\delta_{r_{V1}}$, all the starting vortices appear to grow in extent until x/d = 5. This starting vortex for cases b, c and e at x/d = 10 appear to decrease or remain almost the same. For case d (DP, Δ_p = 0.5s) the extent increases while for case f an increase is observed until x/d = 5 and a clear decrease in radial extent is observed at x/d = 15. Figure. 3.13 shows the radial extent of the starting vortex corresponding to the second puff $\delta_{r_{V2}}$, for different axial locations x/d = 1, 5, 10, 15. The increment in radial extents of starting vortices is observed for all cases c –f. The radial extents for case c and case d were seen to increase until x/d = 15 and the highest increment in radial extent was found for case e (Δ_p = 0.7s) whereas a decrease in radial extent is seen at x/d = 15. This observation indicates that there are interactions between the starting vortices of first and second puff, and a more detailed investigation is necessary to establish nature of this interaction.
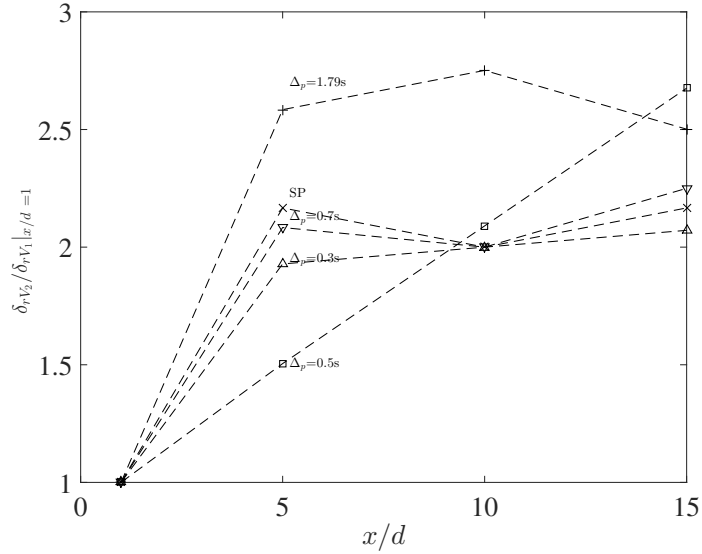
Figure 3.12. The radial extent of the starting vortex corresponding to first puff (– –). The x – ordinate is the non-dimensional axial location x/d , y – ordinate is the non-dimensional radial extent of starting vortex $\delta_{rV_1}/\delta_{rV_1}|_{x/d=1}$ for x/d =15, Legend: $\times$ Case b: SP, Single puff, $\triangle$ Case c: DP, Δ_p ≈ 0.3s , $\square$ Case d: DP, $\Delta_p \approx 0.5$s , $\triangledown$ Case e: DP, $\Delta_p \approx 0.7$s, + case f: DP, $\Delta_p \approx 1.79$s.
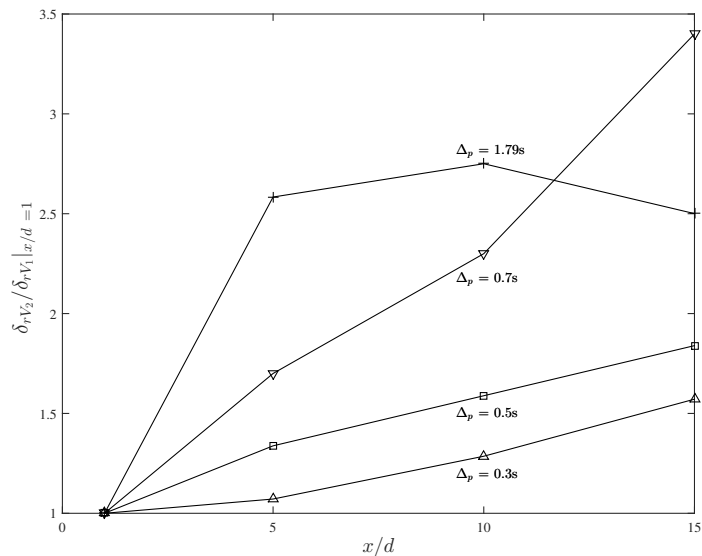
Figure 3.13. The radial extent of the starting vortex corresponding to second puff (-). x – ordinate is the axial location, y – ordinate is the non-dimensional radial extent of starting vortex $\delta_{rV_2}/\delta_{rV_2}|_{x/d=1}$ for x/d =15, Legend: $\triangle$ Case c: DP, $\Delta_p \approx 0.3$s, $\square$ Case d: DP, $\Delta_p \approx 0.5$s, $\triangledown$ Case e: DP, $\Delta_p \approx 0.7$s, + case f: DP, $\Delta_p \approx 1.79$s.

3.6 Evolution of Puff Volume

To get further understanding of the evolution of the puff its change in volume is considered. An estimate of the volume change as the puff develops was obtained by considering the area enveloped by the velocity magnitude contour when the velocity is 20% of the normalized velocity V/V_j, as shown in Fig. 3.14. The volume shown here is normalized with respect to the volume at $x/d = 1$. To obtain an estimate of the robustness of this result, the 30% V/V_j velocity contour based volume estimation is plotted in Fig. 3.15. The puff volume is seen to increase for all cases as it evolves with increment in the axial location immediately after the jet exit $(x/d = 5)$. This growth in volume continues at the axial locations $x/d = 1$, 5, 10 and 15 for cases $\Delta_p \leq 0.7$s (Cases c – e) as seen in Fig. 3.14. However, at $x/d = 15$ for Case b (SP) and case f (DP, $\Delta_p = 1.79$s) a drop in the volume is evident. This drop indicates the start of the decay of the puff because of dissipation. Considering the results in Fig. 3.15 (estimated based on 30% V/V_j), a similar result is seen except that at $x/d = 15$ Cases e and c also appear to slightly reduce in volume.

The double puff with $\Delta_p = 1.79$s (Case f) has the highest volume growth immediately downstream of the jet exit $(x/d \leq 10)$. When viewed in conjunction with the starting vortex evolution, as shown in Figures. 3.12 and 3.13, this outcome suggests that there exists an interaction between the puffs that causes this rapid growth. Hence, for an application such as fuel injection, where rapid mixing is desired, this behavior appears to be the most efficient Δ_p. However when the time separation is shorter, i.e., $\Delta_p \leq 0.5$s, the puff persists for a much longer downstream distance. This result indicates that there again exists

an interaction between the puffs, which results in the persistence of the puffs to longer distances.
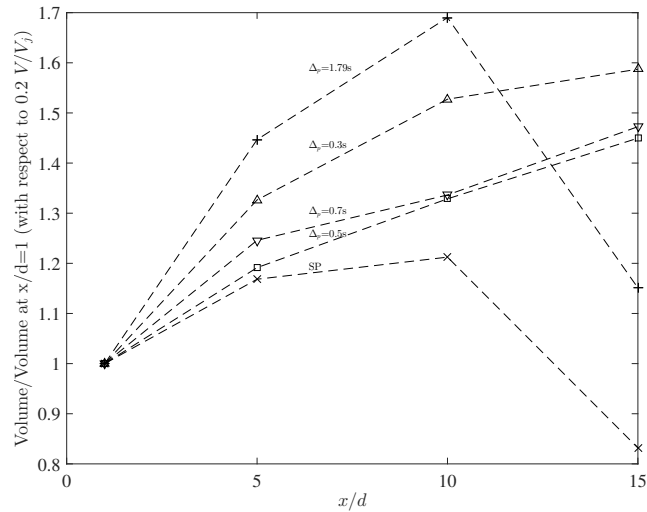
Figure 3.14. Non-dimensional volume with respect to 0.2 V/V_j at different axial locations. x-ordinate is the non-dimensional axial location x/d, y-ordinate is the non-dimensional volume respectively. Legend: $\times$ Case b: SP, Single puff, $\triangle$ Case c: DP, $\Delta_p \approx 0.3$s, $\square$ Case d: DP, $\Delta_p \approx 0.5$s, $\triangledown$ Case e: DP, $\Delta_p \approx 0.7$s, + case f: DP, $\Delta_p \approx 1.79$s.
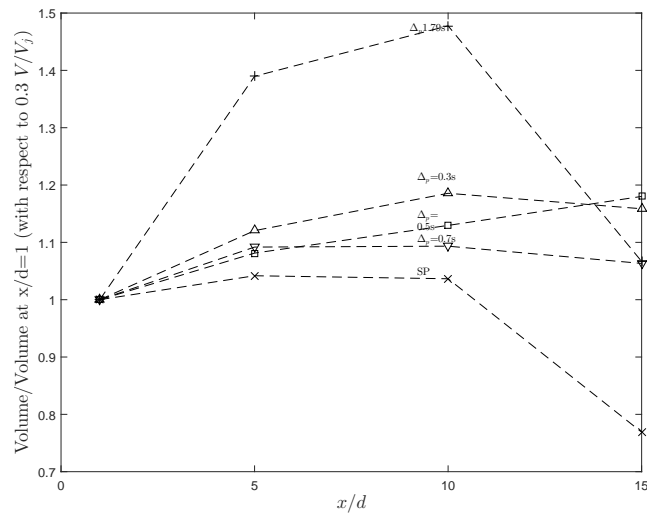
Figure 3.15. Non-dimensional volume with respect to 0.3 V/V_j at different axial locations. x-ordinate is the non-dimensional axial location x/d, y-ordinate is the non-dimensional volume respectively. Legend: $\times$ Case b: SP, Single puff, $\triangle$ Case c: DP, $\Delta_p \approx 0.3$s, $\square$ Case d: DP, $\Delta_p \approx 0.5$s, $\triangledown$ Case e: DP, $\Delta_p \approx 0.7$s, + case f: DP, $\Delta_p \approx 1.79$s.

3.7   Discussion

Based on the observations presented in this chapter dual puffs can be broadly classified into two flow categories. These categories are based on the following specific observations. The expansion of dual puff with time interval $\Delta_p \leq 0.5$ s is seen to increase for all axial locations considered. This indicates that dual puffs that are separated by this time scale i.e., $\Delta_p V_j/d = 430$ persist for much longer distances than single puffs or puffs with longer separation ($\Delta_p = 1.79$ s). This has some significance as a volcano or coughs for example ejecting dual puffs with this time scale will persist for much longer distances. As a note, dual puffs with $\Delta_p = 0.7$ s, 0.3 s are observed to behave similarly to that of $\Delta_p = 0.5$ s. However, dual puffs with longer separation $\Delta_p = 1.79$ s i.e. time scale of $\Delta_p V_j/d = 1540$ show a rapid increase in volume very close to the jet exit $x/d \leq 5$. This increase is much more rapid than any of the cases considered. This appears to indicate that for applications that require rapid mixing with the ambient (fuel injectors for example) it is desirable to divide the total ejected volume into two puffs separated by $\Delta_p V_j/d = 1540$ than a single puff of the same volume. Hence dual puffs can be broadly divided into these two categories i.e puffs with $\Delta_p V_j/d = 430$ which persist for longer distances while puffs with $\Delta_p V_j/d = 1540$ rapidly mix with the ambient.

4. Conclusions and Future Work

The studies on momentum driven unsteady jets have primarily focused on single ejection events (single puffs). This work focuses on dual puffs in which two volumes of fluid (dual puffs), separated by time Δ_p were ejected into ambient. An experimental framework to study momentum driven unsteady jet was built and was used to generate single puff and dual puffs. The mean velocity of these flow fields was measured using hot-wire anemometry over several axial locations $x/d = 1 - 15$. Four different double puffs were considered with the time separation between the two puffs $\Delta_p = 0.3s$, $0.5s$, $0.7s$ and $1.79s$. The dual puffs studied were compared with both a steady jet and single puffs. Complementary flow visualizations were also carried out. The dominant flow structure or coherent structure in the flow field was the starting vortex corresponding to the first and second puff. Depending on the time separation between the two puffs it was found that the flow field evolved differently. It is suspected that this difference in evolution is due to the interaction between the two starting vortices. Some of the main conclusions of this work are presented below.

1. The radial extents (based on the maximum mean velocity) for the case of the puffs was found to be greater when compared with a steady jet for all axial locations until $x/d = 10$ and approximately the same at $x/d = 15$.

2. There were significant differences in the evolution of the starting vortices themselves when comparing the various double puffs, which is a further indication that the evolution of the flow field is dependent on the interaction between the starting vortices.

3. When the time separation is of order $\Delta_p \leq 0.5$ s ($\Delta_p V_j/d = 430$) the dual puff persists for a much longer distances when compared to a single puff or dual puffs with larger time separation ($\Delta_p = 1.79$ s.) This indicates that there again exists an interaction between the puffs which results in this persistence of the puffs.

4. The double puff with the longest time separation $\Delta_p = 1.79$ s ($\Delta_p V_j/d = 1540$) has the highest growth in volume immediately downstream of the jet exit ($x/d \leq 10$) and starts to decay at $x/d = 15$. The flow behavior is similar to that of a single puff but the initial growth is much faster than the single puff and the other dual puffs considered.

5. Based on these observations, the dual puffs studied can be categorized into two based on the time scales as follows a) $\Delta_p V_j/d = 430$ and b) $\Delta_p V_j/d = 1540$

These observations have some potential practical implications. Considering a volcano if dual puffs are ejected at the shorter time scales ($\Delta_p V_j/d = 430$) they will presist for longer distances. This implies that the pyroclastic material can potentially be spread over a much larger region or reach the upper atmosphere. Either of these scenarios poses a threat to aviation safety. It noted that volcanic plumes occur at a much larger Reynolds number having a buoyancy as well as a multiphase component. Hence, a natural extension of this study is to investigate multiphase, variable density high Reynolds number unsteady jets.

The higher spreading rate observed at the larger time scale ($\Delta_p V_j/d$ = 1540) has implications for spraying applications such as fluid injection where rapid mixing is desired. In this scenario it appears that it is better to divide the total ejection volume into two consecutive puffs for rapid mixing.

Several observations have been made as part of this work primarily relying on integral quantities. However, to establish the exact flow physics a systematic study relying on multi-point unsteady velocity measurements is needed. Hence it is recommend that a more sophisticated measurement technique namely high-speed particle image velocimetry (PIV) be used to investigate further the internal physics of dual puffs.

References

Abdel-Rahman, A., Chakroun, W., & Al-Fahed, S. (1997). Lda measurements in the turbulent round jet. *Mechanics Research Communications*, *24*(3), 277–288.

Bajpai, S. K. (n.d.). *Experimental study of an unsteady, axisymmetric, turbulent jet.* (Unpublished doctoral dissertation). Indian Institute of Technology, Bombay.

Boguslawski, L., & Popiel, C. O. (1979). Flow structure of the free round turbulent jet in the initial region. *Journal of Fluid Mechanics*, *90*(03), 531–539.

Bourouiba, L., Dehandschoewercker, E., & Bush, J. W. (2014). Violent expiratory events: on coughing and sneezing. *Journal of Fluid Mechanics*, *745*, 537–563.

Chevray, R., & Tutu, N. (1978). Intermittency and preferential transport of heat in a round jet. *Journal of Fluid Mechanics*, *88*(01), 133–160.

Chojnicki, K., Clarke, A., Adrian, R., & Phillips, J. (2014). The flow structure of jets from transient sources and implications for modeling short-duration explosive volcanic eruptions. *Geochemistry, Geophysics, Geosystems*, *15*(12), 4831 - 4845.

Chojnicki, K., Clarke, A., Phillips, J., & Adrian, R. (2015). Rise dynamics of unsteady laboratory jets with implications for volcanic plumes. *Earth and Planetary Science Letters*, *412*, 186–196.

Fagents, S. A., Gregg, T. K., & Lopes, R. M. (2013). Modeling volcanic processes: the physics and mathematics of volcanism.

Fellouah, H., Ball, C., & Pollard, A. (2009). Reynolds number effects within the development region of a turbulent round free jet. *International Journal of Heat and Mass Transfer*, *52*(17), 3943–3954.

Ghaem-Maghami, E., & Johari, H. (2007). Velocity field of isolated turbulent puffs. *Collection of Technical Papers - 45th AIAA Aerospace Sciences Meeting*, *22*, 15701 - 15719.

Ghaem-Maghami, E., & Johari, H. (2010). Velocity field of isolated turbulent puffs. *Physics of Fluids (1994-present)*, *22*(11), 115105.

Gupta, Lin, C.-H., & Chen, Q. (2009). Flow dynamics and characterization of a cough. *Indoor air*, *19*(6), 517–525.

Hussein, H. J., Capp, S. P., & George, W. K. (1994). Velocity measurements in a high-reynolds-number, momentum-conserving, axisymmetric, turbulent jet. *Journal of Fluid Mechanics*, *258*, 31–75.

Iqbal, M., & Thomas, F. (2007). Coherent structure in a turbulent jet via a vector implementation of the proper orthogonal decomposition. *Journal of Fluid Mechanics*, *571*, 281–326.

Kwon, S.-B., Park, J., Jang, J., Cho, Y., Park, D.-S., Kim, C., . . . Jang, A. (2012). Study on the initial velocity distribution of exhaled air from coughing and speaking. *Chemosphere*, *87*(11), 1260 - 1264.

Meisser, S. (2011). Particle and trace gas measurements of eyjafjallajökull 2010. , 1-56.

Myagkov, N. (1998, apr). Model of a strong volcanic blast and a method of estimating the mass ejected. *Geophysical Journal International*, *133*(1), 209–211.

Nishi, M., Ünsal, B., Durst, F., & Biswas, G. (2008). Laminar-to-turbulent transition of pipe flows through puffs and slugs. *Journal of Fluid Mechanics*, *614*, 425–446.

Nobes, J., Mi, DS, & Nathan, G. (2001). Influence of jet exit conditions on the passive scalar field of an axisymmetric free jet. *Journal of Fluid Mechanics*, *432*, 91–125.

Panchapakesan, N., & Lumley, J. (1993). Turbulence measurements in axisymmetric jets of air and helium. part 1. air jet. *Journal of Fluid Mechanics*, *246*, 197–223.

Parshley, P. F., Kiessling, P. J., Antonius, J. A., Connell, R., Miller, S. H., & Green, F. H. (1982). Pyroclastic flow injury: Mount st. helens, may 18, 1980. *The American Journal of Surgery*, *143*(5), 565–568.

Quinn, W., & Militzer, J. (1989). Effects of nonparallel exit flow on round turbulent free jets. *International Journal of Heat and Fluid Flow*, *10*(2), 139–145.

Romano, G. (2002). The effect of boundary conditions by the side of the nozzle of a low reynolds number jet. *Experiments in fluids*, *33*(2), 323–333.

Stewart, J., & Turner. (1979). Buoyancy effects in fluids.

Suzuki, Y., & Koyaguchi, T. (2010). Numerical determination of the efficiency of entrainment in volcanic eruption columns. *Geophysical Research Letters*, *37*(5).

Weisgraber, T., & Liepmann, D. (1998). Turbulent structure during transition to self-similarity in a round jet. *Experiments in Fluids*, *24*(3), 210–224.

Wygnanski, I., & Fiedler, H. (1968). Some measurements in the self preserving jet.

Xu, G., & Antonia, R. (2002). Effect of different initial conditions on a turbulent round free jet. *Experiments in Fluids*, *33*(5), 677–683.

A. Dual Puff with Δ_p = 0.3s, Δ_p = 0.7s

A.1 Double Puff, DP, Δ_p = 0.3s

For the Case of dual puff with Δ_p = 0.3s, the second puff exits into the flow domain 0.3 s after the first puff. There is a starting vortex corresponding to the first puff as well as the second puff as shown in Fig. A.1. These starting vortices are observed in the pseudo contour plot shown in Fig.A.2. This location corresponds to the potential core of the puff and the radial extent r/d of both the starting vortices are in the range - 0.6 – 0.6 at this axial location.

With increase in downstream distance at x/d = 5, the radial extent of the starting vortices corresponding to each puff are seen to increase in size which is a result of entrainment. The radial extent of the starting vortex corresponding to the first puff $\delta_{r_{V1}}$, is shown in Figures. A.1 and A.2. It was found to increase relative to that at x/d =1. For Case c, the radial extent is approximately 1.9 times of that at x/d = 1. The radial extent of the starting vortex corresponding to the second puff $\delta_{r_{V2}}$, is shown in Figures. A.1 and A.2. Its value was found to increase similar to that of first starting vortex. For Case c this is approximately 1.2 times of that at x/d = 1. However, the temporal extent is seen to decrease or remain almost the same as observed in the pseudo contour shown in Fig.A.2.

At x/d = 10, the puff expands greater than the previous upstream location which is a result of entrainment which inturn leads to instability in the flow field. The peak velocity

of the starting vortex corresponding to the second puff was 70% V/V_j of the first puff. The radial extent of the starting vortex corresponding to the first puff $\delta_{r_{V1}}$, is shown in Fig. A.2 and is approximately twice that at $x/d = 1$ and approximately 1.03 times of that at $x/d = 5$. The radial extent of the starting vortex corresponding to the second puff $\delta_{r_{V2}}$, was found to be approximately 1.25 times of that at $x/d = 1$ and approximately 1.2 times of that at $x/d = 5$.

Puff structure is fully breaken down at this axial location and flow domain is fully turbulent. The radial extent of the starting vortex corresponding to the first puff $\delta_{r_{V1}}$, is found to be approximately 2.07 times of that at $x/d = 1$ and approximately 1.07 times with respect to $x/d = 5$ whereas it is approximately 1.03 times of that at $x/d = 10$. The radial extent of the starting vortex corresponding to the second puff $\delta_{r_{V2}}$, is approximately 1.5 times of that at $x/d = 1$ and approximately 1.46 times of that at $x/d = 5$ whereas it is approximately 1.2 times of that at $x/d = 10$. The temporal extent corresponding to $20\%V/V_j$ which is used as a representative volume is seen decrease or remain almost the same at different axial locations as shown in Fig.A.2.
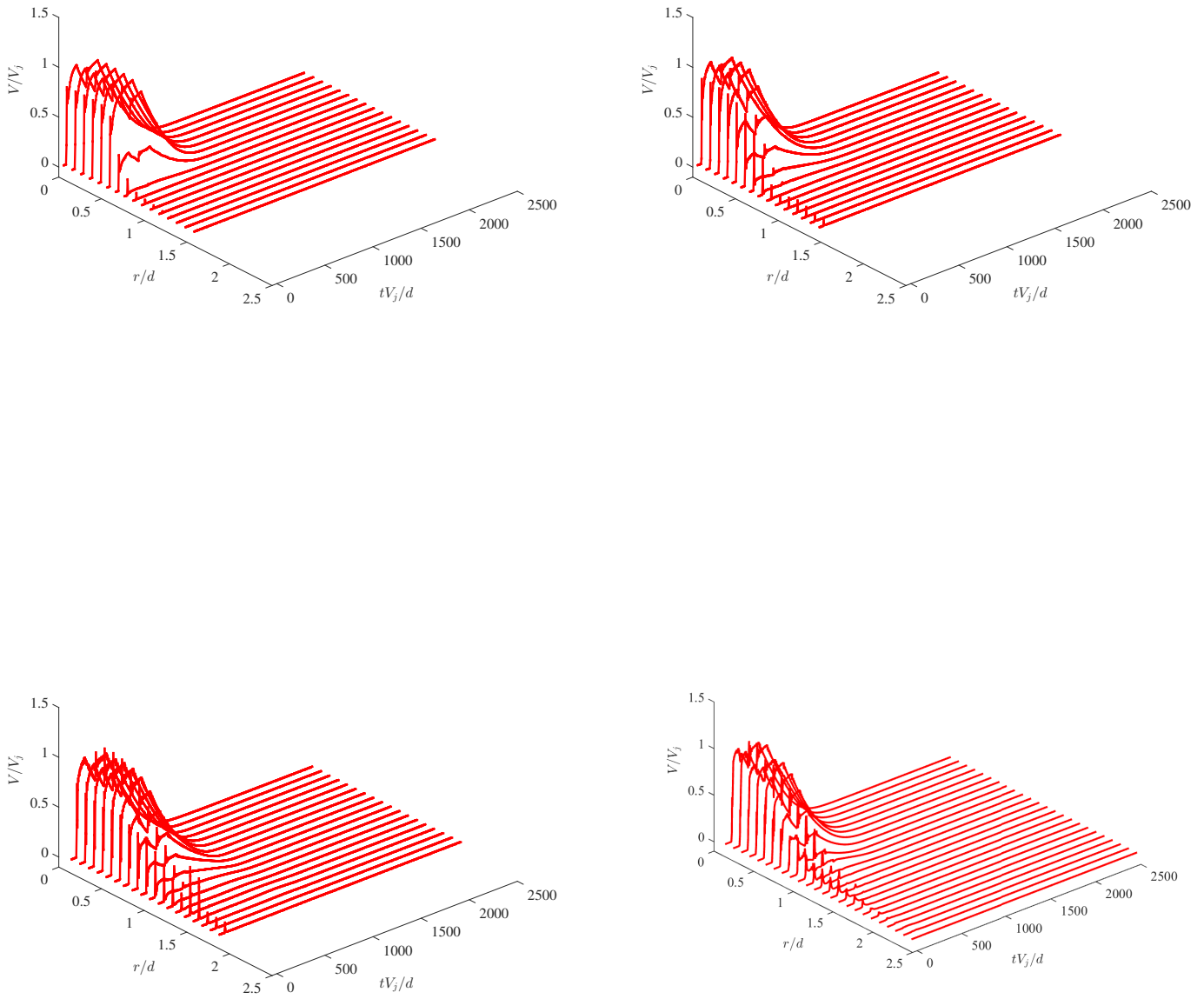
Figure A.1. Case c (Double puff, Δ_p = 0.3s): Normalized axial velocities at axial locations from x/d = 1 to x/d = 15. x – ordinate is the non-dimensional radial location r/d, y – ordinate is the non-dimensional time tV_j/d , z – ordinate is the non dimensional velocity magnitude V/V_j respectively. The color contours are the magnitudes of the non-dimensional velocity V/V_j.
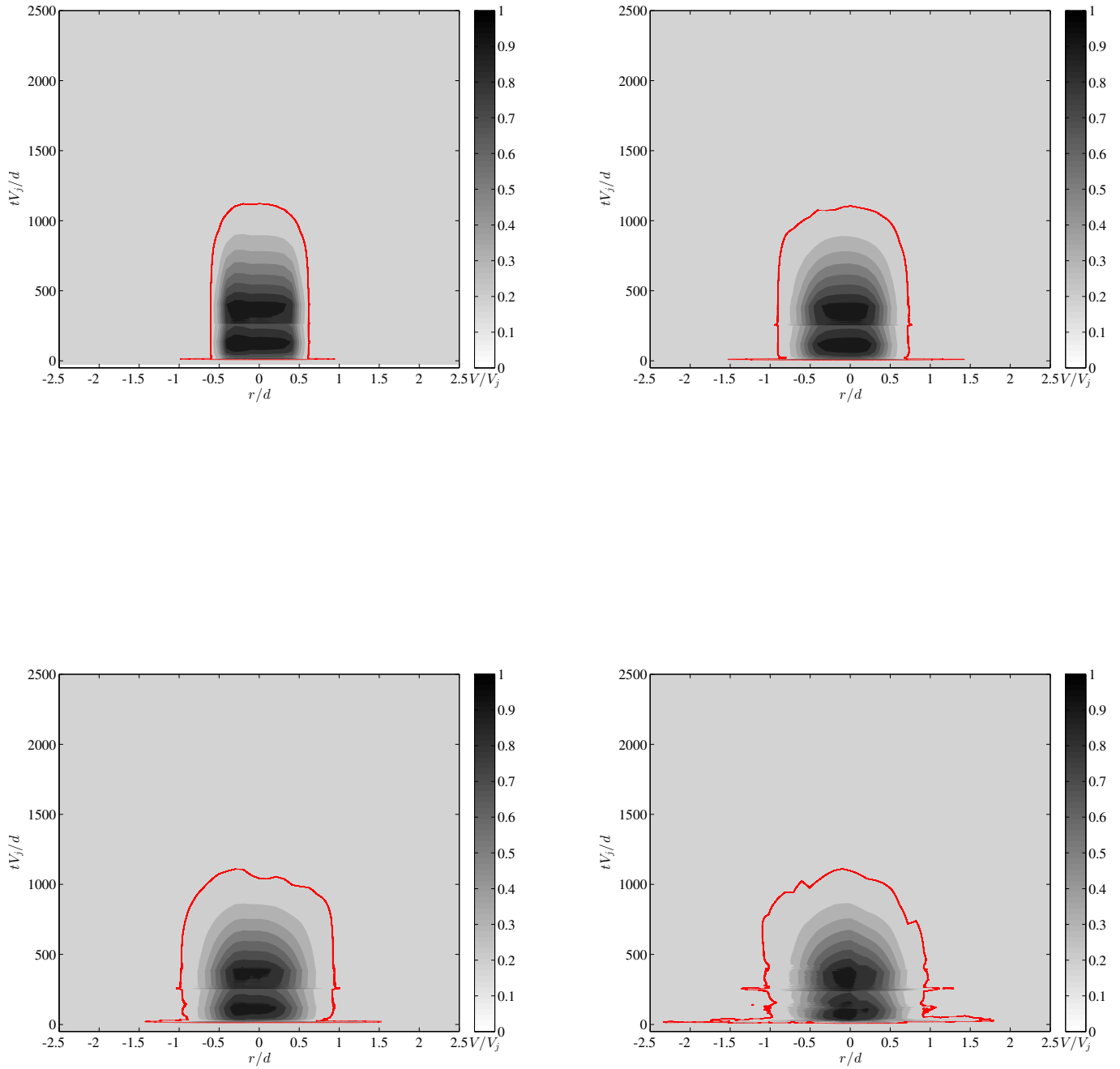
;

Figure A.2. Case c (Double puff, $\Delta_p = 0.3$s): Pseudo contour plot of normalized axial velocities at axial locations from $x/d = 1$ to $x/d = 15$. x – ordinate is the non-dimensional radial location r/d, y – ordinate is the non-dimensional time tV_j/d. The color contours are the magnitudes of the non-dimensional velocity V/V_j.

A.2 Double Puff, DP, Δ_p = 0.7s

For the dual puff with Δ_p = 0.7s i.e., when the second puff exits the nozzle 0.7 s after the first puff the three-dimensional velocity profile and two-dimensional velocity contour plot are shown in Figures. A.3 and A.4. The second puff is injected into the flow domain when the first puff has a velocity which was 20% of the maximum velocity i.e. $V/V_j \approx$ 0.1 of the first puff. The radial extent of the puff is seen to be between -0.6 – 0.6 similar to the previous cases. The temporal extent of the first puff ($tV_j/d \approx 20$ to $tV_j/d \approx 700$) is decreasing or approximately equal to the temporal extent of the second puff ($tV_j/d \approx 700$ to $tV_j/d \approx 1400$).

Entrainment of ambient air as the puff evolves downstream is evident analogous to previous cases. This in-turn leads to the increase in radial expansion of the puff. The peak velocity of the starting vortex corresponding to the second puff was 20% V/V_j of the first puff. The radial extent of the starting vortex corresponding to the the first puff $\delta_{r_{V1}}$, is approximately 2.1 times of that at $x/d = 1$ and this is higher than the case c and case d. The radial extent of the starting vortex corresponding to the second puff $\delta_{r_{V2}}$, is approximately 1.7 times of that at $x/d = 1$.

Mean velocity field and pseudo contour of the dual puff at $x/d = 10$ are shown in Figures.A.3 and A.4 and the peak velocity of the starting vortex corresponding to the second puff is 20% V/V_j of the first puff. The radial extent of the starting vortex corresponding to the first puff $\delta_{r_{V1}}$, is found to be approximately twice that at $x/d = 1$ and approximately 0.96 times of that at $x/d = 5$. This behavior is observed to be the same for all the cases ($\leq$

0.7 s) for the first puff except for case d. The radial extent of starting vortex corresponding to the second puff $\delta_{r_{V2}}$, is found to be approximately 2.29 times of that at $x/d = 1$ and approximately 1.35 times of that at $x/d = 5$. The temporal extent however, decreased or remained almost the same when compared to $x/d = 5$ and $x/d = 1$.

At $x/d = 15$, the flow is fully turbulent and the peak velocity of the second puff similarly is 20% V/V_j of the first puff. The radial extent of the starting vortex corresponding to the first puff $\delta_{r_{V1}}$, is found to be approximately 2.25 times of that at $x/d = 1$ and decreases approximately 1.08 times of that at $x/d = 5$ whereas it is approximately 1.12 times of that at $x/d = 10$. The radial extent of the starting vortex corresponding to the second puff $\delta_{r_{V2}}$, is approximately 3.4 times of that at $x/d = 1$, twice that at $x/d = 5$ and approximately 1.47 times of that at $x/d = 10$.
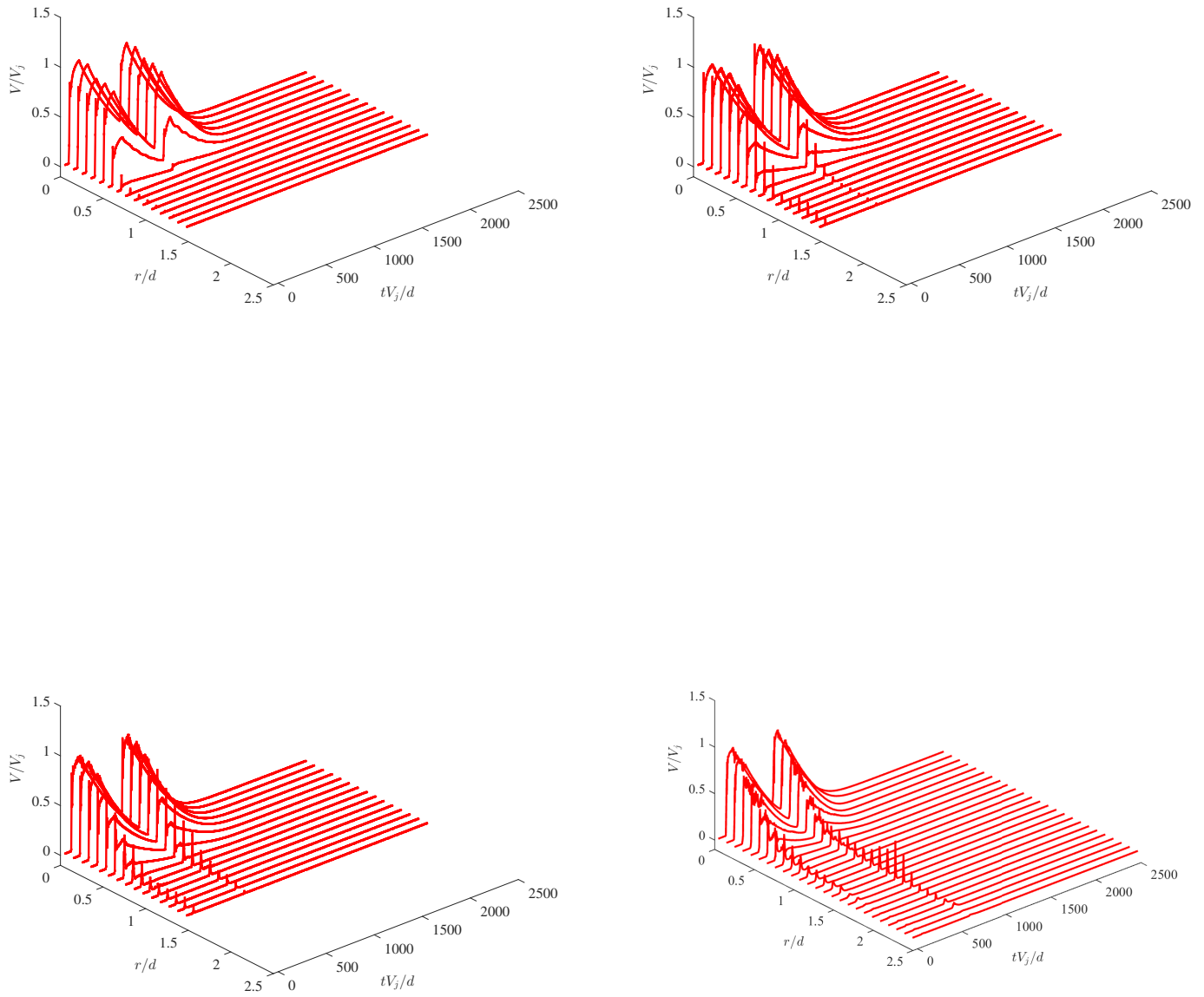
Figure A.3. Case e (Double puff, Δ_p = 0.7s): Normalized axial velocities at axial locations from x/d = 1 to x/d = 15. x – ordinate is the non-dimensional radial location r/d, y – ordinate is the non-dimensional time tV_j/d , z – ordinate is the non dimensional velocity magnitude V/V_j respectively. The color contours are the magnitudes of the non-dimensional velocity V/V_j.
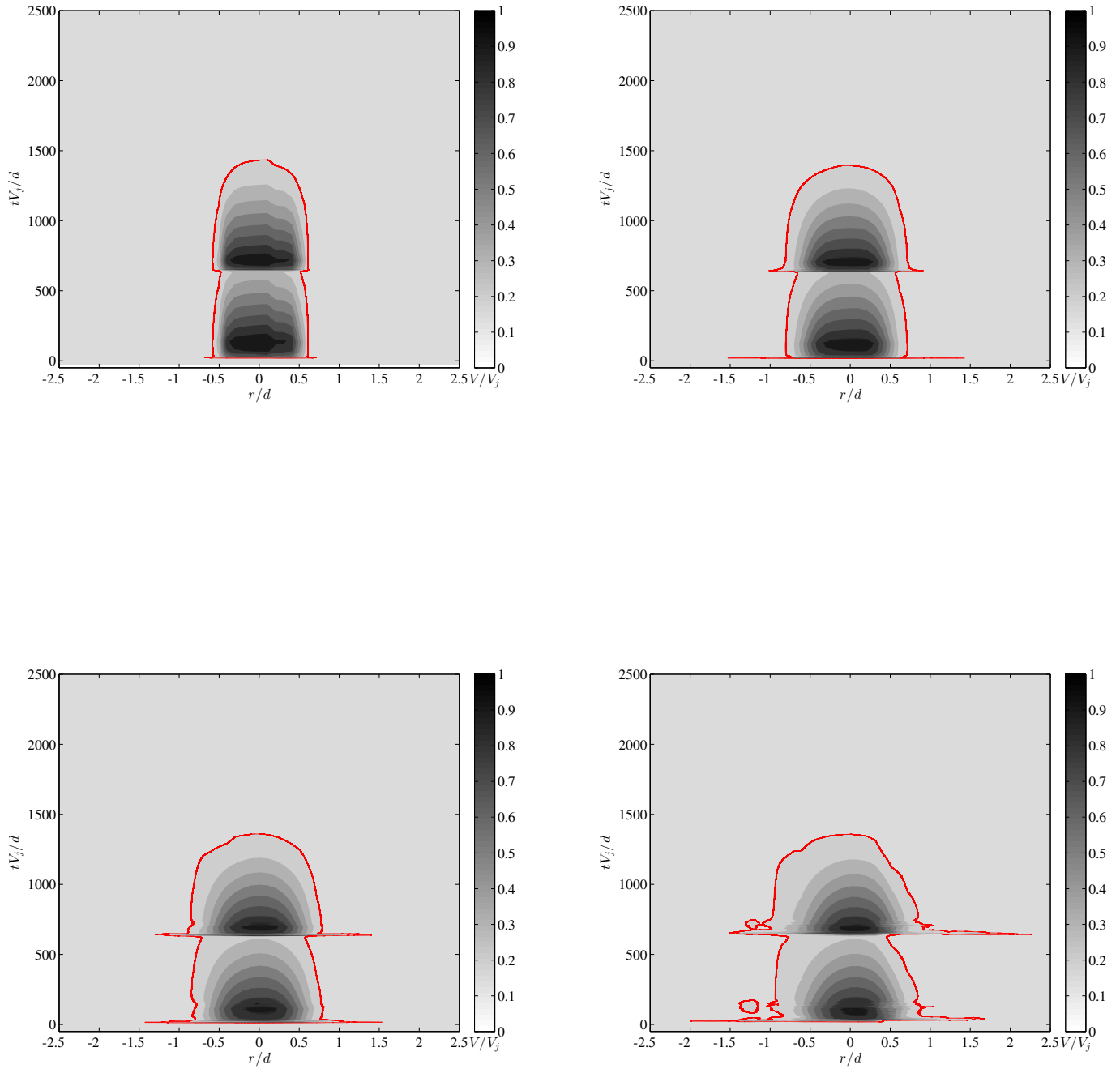
Figure A.4. Case e (Double puff, Δ_p = 0.7s): Pseudo contour plot of normalized axial velocities at axial locations from x/d = 1 to x/d = 15. x – ordinate is the non-dimensional radial location r/d, y – ordinate is the non-dimensional time tV_j/d. The color contours are the magnitudes of the non-dimensional velocity V/V_j.

B. ERROR QUANTITIES FOR PRESSURE VARIATION.

Table B.1.: Case b (Single Puff, SP)

SP, Single Puff	$x/d=1$	$x/d=5$	$x/d=10$	$x/d=15$
Mean (P_o max)	0.0506	0.0505	0.0509	0.0593
Std. Dev (P_o max)	0.0017	0.0016	0.0017	0.0026
Mean (max std)	0.0034	0.0033	0.0035	0.0033
Max (max std)	0.00128	0.0046	0.0121	0.0063

Table B.2.: Case c (Double puff, $\Delta t=0.3s$)

DP, $\Delta t=0.3s$	$x/d=1$	$x/d=5$	$x/d=10$	$x/d=15$
Mean (P_o max)	0.0622	0.0620	0.0627	0.0627
Std. Dev (P_o max)	0.0026	0.0028	0.0027	0.0028
Mean (max std)	0.0247	0.0247	0.0249	0.0249
Max (max std)	0.0270	0.0288	0.0273	0.0274

Table B.3.: Case d (Double puff, $\Delta t=0.5s$)

DP, $\Delta t=0.5s$	$x/d=1$	$x/d=5$	$x/d=10$	$x/d=15$
Mean (P_o max)	0.0656	0.0654	0.0656	0.0645
Std. Dev (P_o max)	0.0023	0.0024	0.0023	0.0021
Mean (max std)	0.0306	0.0304	0.0305	0.0299
Max (max std)	0.0323	0.0321	0.0318	0.0312

Table B.4.: Case e (Double puff, $\Delta t=0.7s$)

DP, $\Delta t=0.7s$	$x/d=1$	$x/d=5$	$x/d=10$	$x/d=15$
Mean (P_o max)	0.0615	0.0619	0.0624	0.0623
Std. Dev (P_o max)	0.0029	0.0030	0.0029	0.0031
Mean (max std)	0.0307	0.0308	0.0309	0.0309
Max (max std)	0.0331	0.0327	0.0330	0.0329

Table B.5.: Case f (Double puff, Δt=1.79s)

DP, Δt=1.79s	x/d=1	x/d=5	x/d=10	x/d=15
Mean (P_o max)	0.0620	0.0625	0.0624	0.0635
Std. Dev (P_o max)	0.0023	0.0022	0.0020	0.0021
Mean (max std)	0.0031	0.0030	0.0030	0.0030
Max (max std)	0.0050	0.0044	0.0046	0.0045

C. CALIBRATIONS
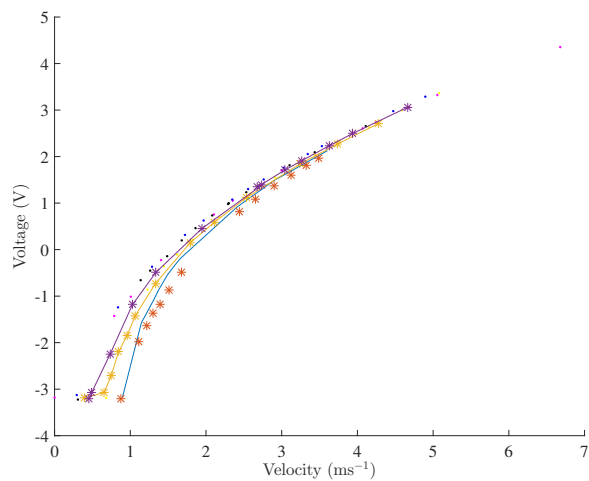

Figure C.1.Calibration curve of the hot-wire probe. x – ordinate is the Velocity in ms^{-1}, y – ordinate is the Voltage in volts respectively.
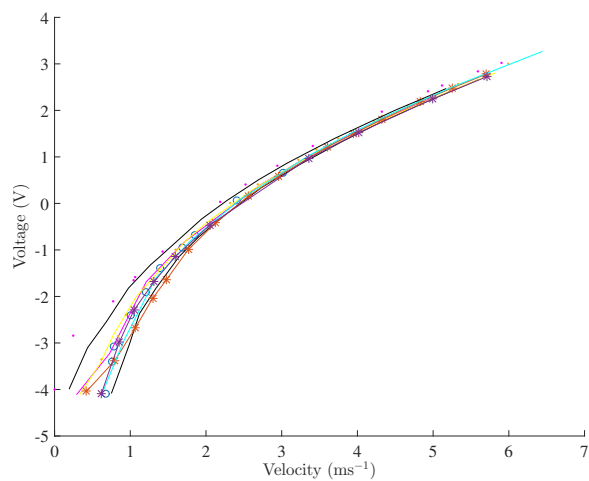

Figure C.2.Calibration curve of the hot-wire probe. x – ordinate is the Velocity in ms^{-1}, y – ordinate is the Voltage in volts respectively.